Landslide initiation susceptibility, Prince of Wales Island

Dan Miller, TerrainWorks

January 28, 2021

Executive summary.

Newly available Lidar DEMs together with the Tongass National Forest Landslide Inventory, Soil Inventory, and Activity Tracking database provide data for a unique examination of how topography, soil types, and timber-harvest history are associated with mapped landslide locations. These associations are determined in terms of landslide density: the number of landslide initiation sites per unit area measured as functions of these attributes. If these three attributes are important determinants of landslide location, then observed landslide density over any area depends on the unique combination of topography, soil type, and harvest history found over that area. This analysis seeks to separate the effects of each. The sequence of landslide occurrences and timber harvests recorded in the landslide and activity-tracking databases were overlain on DEM-derived topography and polygons from the soil inventory to quantify changes in landslide density with each combination of variables. Relationships are quantified in terms of proportional change from the mean landslide density observed over the entire study area. Topography is a primary factor, with certain terrain exhibiting densities from 3 to 15 times greater than the average. Timber harvest is also associated with increased landslide density, with density in young stands from 15 to 20 times higher than the mean. The apparent increase in density drops off with increasing stand age to reach levels associated with unharvested zones in about 50 to 60 years. Certain soil types, primarily those overlying till, exhibit landslide densities about twice the mean value.

Susceptibility to landslide initiation is quantified in two ways: 1) in terms of spatial variations in landslide density (or rate by dividing density by the time period of analysis), and 2) by dividing the landscape into zones encompassing a given proportion of the observed landslide initiation sites, ranked from highest density to lowest.

Two methods of determining landslide initiation locations were used: 1) automated placement at the least-stable point (as determined by topography) within the upper portion of each mapped landslide polygon, and 2) manual placement from aerial photo interpretation provided with the landslide inventory. These two methods produce associations with topography that exhibit similar spatial patterns, with high and low density values occupying the same terrain, but with magnitudes that differ by about a factor of three in areas with the highest inferred densities. When translated to the area encompassing a given proportion of landslides, the automated point placement appears to better resolve landslide sites, with less area in high-susceptibility zones. This is a consequence of the method used to locate landslide initiation sites on a map and the implications for interpretation of model results is unclear. This discrepancy points to a need for assessing the appropriate spatial scale for susceptibility assessments.

Introduction

Timber lands in the Tongass National Forest include areas prone to landsliding. Landslides in southeast Alaska predominately involve failure of relatively shallow soils – generally 2 meters or less – overlying more competent substrates, such as till or bedrock (Swanston, 1969). The rate of these shallow landslides, in terms of number per unit area per year, have been estimated to be about 3.5 times greater in logged areas than in unlogged areas (Swanston and Marion, 1991). This has motivated efforts to identify the factors associated with landslide occurrence, to understand the physical mechanisms involved, and to delineate areas prone to landsliding and susceptible to management-induced changes in landslide rate (Johnson and Wilcock, 1998; Johnson et al., 2000; Swanston, 1997; Wu and Swanston, 1980). This study builds on previous work, but now uses a substantial new source of elevation data provided by the Lidar-derived DEMs for Prince of Wales Island. These DEMs, together with the Tongass National Forest Landslide Inventory, Soil Inventory, and Management Activity GIS coverage, provide a unique data set for examining the association of landslide occurrence with harvest activity and substrate types.

Landslide scars persist for some time, so the number of new landslide scars observed in a sequence of air photos indicates the number of landslides that occurred during the period between successive photos[1]. The number of landslides divided by the area surveyed gives landslide density as number per unit area. Dividing the density by the time over which those landslides occurred provides a landslide rate: number per unit area per unit time. Using landslide inventories mapped from aerial photos, Swanston and Marion (1991) observed 1277 landslides distributed over 41,503 km^2 giving a density of 0.031 landslides per km^2 in areas undisturbed by timber harvest. From the same photo inventory they observed 103 landslides over the 980 km^2 of land where timber harvest had occurred, giving a density of 0.105 landslides per km^2. The photos in which new landslides were observed spanned 20 years, giving rates of 0.00154 landslides/km^2/yr in unharvested areas versus 0.00526 landslides/km^2/yr in harvested areas: over that period of time, landslides in harvested zones occurred at a rate 3.4 times greater than in unharvested zones. This is consistent with studies elsewhere that also find increases in apparent landslide rate in harvested zones relative to unharvested zones (Amaranthus et al., 1985; Guthrie, 2002; Imaizumi et al., 2008; Miller and Burnett, 2007; Swanson and Dyrness, 1975; Wolfe and Williams, 1986).

The magnitude of the increase varies, however, from place to place. Response to timber harvest can differ regionally from basin to basin (Brardinoni et al., 2002; Brardinoni et al., 2003) and, within a basin, with time since harvest (Schmidt et al., 2001) and across different terrains within a basin. Swanson and Dyrness (1975) provide an illustrative example. They examined landslides occurring over an approximately 20-year period (1950 - 1974) in the H. J. Andrews Experimental Forest in western Oregon. The experimental forest can be divided into two regions: a higher elevation zone spanning 30.8 km^2 underlain by relatively pristine lava flows and a lower elevation zone spanning 33.4 km^2 underlain by more weathered volcaniclastic rocks. Clear-cut logging and road construction occurred within both zones over the period of observations, affecting 21.1% of the upper zone and 30.6% of the lower zone. Over that period, two road-related landslides occurred in the upper zone with none in the forested or clear-cut areas. In the lower zone, 32 landslides occurred in the forested area, 36 in the clear cut area

---

[1] Actually, the number of landslides that can be seen in the photos. Smaller landslides may be missed and the proportion missed may be larger in areas with extensive tree cover. Comparison of field and aerial-photo surveys indicate that a substantial portion of landslides may not be visible in aerial photographs (Brardinoni et al., 2003).

and 71 along road right-of-ways. In the lower zone, harvest activities resulted in a 3-times increase in landslide rate (in terms of number per km^2 per year) in clear cuts, relative to forested areas, and a 31.5 times increase along roads. This is dramatically different than what was observed in the upper, more stable terrain.

These studies point to three primary factors associated with this variable response to timber harvest: differences in topography, differences in the time since harvest within managed forests, and differences in soil and substrate properties. Slope gradient and contributing area are among the topographic attributes associated with landslide locations (Buma and Johnson, 2015; Swanston, 1997), so differences in topography from site to site may result in differing responses to timber harvest (Brardinoni et al., 2002). Landslide density is found to vary with time since harvest (Imaizumi et al., 2008; Sidle, 1992; Ziemer and Swanston, 1977), so the temporal and spatial distribution of stand ages within harvested sites over the area of observation will also affect observed differences in landslide density between harvested and unharvested areas. The example from Swanson and Dryness described above suggests that the provenance of soils that fail and properties of the underlying substrate can exert a strong influence on relative stability and response to timber harvest.

To characterize susceptibility to landslide initiation and sensitivity to timber harvest, we need to separate the influence of these multiple confounding factors. This can be done for idealized cases using simulation models, as illustrated by Dhakal and Sidle (2003), but my goal here is to seek empirical associations using observed and measured values. We need 1) landslide locations and dates, 2) harvest unit locations and dates, and 3) elevation data with which to calculate topographic attributes. For this study, the Tongass National Forest landslide inventory and Activity Tracking Polygons provide the first two and the newly collected Lidar elevation data for Prince of Wales Island in Southeast Alaska provides the third.

Landslide density as a measure of susceptibility

I seek to directly relate a measurable indicator of landslide-initiation potential, the dependent variable in this analysis, to three independent variables: topography, stand age (time since harvest), and mapped soil type (as an indicator of potential spatial variation in material properties). If landslide density for a certain type of terrain is known, the probability that a landslide will be found within any zone within that terrain is density multiplied by the area of interest. Number of landslides per unit area – density – provides a quantitative measure of susceptibility. The probability that a randomly placed point will encounter a landslide is proportional to density. For two sites, the first in an area with twice the landslide density as the second, the probability that site one is within 100m of a landslide initiation point is twice that of second.

Density divided by the time over which the observed landslides occurred provides an estimate of rate. The number of landslides likely to occur within any delineated zone over some specified time is rate multiplied by area multiplied by time. Rate, derived from density, provides a measurable and quantitative indicator of potential. For two sites, the first in an area with twice the landslide rate as the second, the probability that site one will experience a landslide is twice that of site two.

The analyses I present here will focus on landslide density, with the understanding that density is proportional to rate.

Topographic weighting

I'll focus first on topography and describe below how it can be related to landslide density. First, however, I want to describe the concept of weighting. Consistent with the terminology I've used with the Sitka Report and the work Kelly Burnett and I did in Oregon (Miller and Burnett, 2007), I'll refer to a topographic measure potentially related to landslide initiation as a topographic index. We will look at how this index is related to landslide density. In a simple case, for example, consider an index consisting of slope gradient. We can parse the landscape into slope increments; e.g., 0-10%, 10-20%, etc.. We can then measure the area (count the DEM cells) and count the number of landslides in each increment. Landslide density for a single slope increment is the number of landslides in that increment divided by the area. That density will vary from increment to increment and a weighted mean value over all increments will give the mean density obtained by dividing the total number of landslides by the total area. I'll describe below a more general procedure for relating landslide density to a topographic index, but for now consider that a landslide density value can be calculated for each DEM cell. The number of landslides expected within any portion of the DEM is estimated by summing the product of density and DEM-cell area for all cells within that portion:

$$N_{LS} = \sum_{i}^{n} a\rho_i \tag{1}$$

where N_{LS}= number of landslides initiated over that portion of the DEM, a = area of a DEM cell, ρ_i= landslide density of the ith cell, and the sum is over all n cells within that portion of interest. Now consider that

$$\rho_i = \rho_0 w_{Ti} \tag{2}$$

where ρ_0 is the mean landslide density over the entire n cells and w_{Ti} is a weighting term that reflects the effect of topography for the ith cell. We can then define

$$w_{Ti} = \frac{\rho_i}{\rho_0} \tag{3}$$

and rewrite Equation (1) as

$$N_{LS} = \rho_0 \sum_{i}^{n} (a w_{Ti}) \tag{4}$$

The term $(a w_{Ti})$ is a topographically weighted cell area for the ith cell. The weighted area is larger in more landslide susceptible terrain and smaller in more stable terrain. It is zero where there is no susceptibility to landslide initiation. The sum over all cells is the area of analysis, so the mean value of w_T is one.

Accounting for correlations between independent variables

Stand Age

Now consider effects of stand age. Equation (1) must still hold when ρ_i represents landslide density for the stand age of the ith cell. Again, we can count the number of landslides occurring within a uniform stand age and divide by the area (number of DEM cells) to get an observed density. But we know that the observed density reflects the influence of both stand age and topography. If areas with a stand age

of 5 years occupy more topographically unstable terrain than areas with a stand age of 20 years, then the observed density for a stand age of 5 will be over estimated relative to density for a stand age of 20. We can, however, correct for this by using the topographically weighted area defined in Equation 4:

$$N_{LS} = \sum_{i}^{n} (aw_{Ti}) \rho_{AGEi} \tag{5}$$

where ρ_{AGEi} is the density associated with the stand age found in the ith DEM cell. Grouping cells by stand age we have:

$$(N_{LS})_{AGEj} = \rho_{AGEj} \sum_{i}^{n_j} (aw_{Ti}) \tag{6}$$

where $(N_{LS})_{AGEj}$ is the number of landslides observed over the area with the jth stand age and n_j is the number of DEM cells with the jth stand age. Hence, density for stand age j, adjusted for topography, is found as:

$$\rho_{AGEj} = \frac{(N_{LS})_{AGEj}}{\sum_{i}^{n_j} (aw_{Ti})} \tag{7}$$

There is a complication, in that the spatial distribution of stand ages changes from year to year. What has a stand age of five years this year will have an age of six next year. The spatial and temporal distribution of stand ages is set by the harvest history and each stand age class will occupy a different subset of the topography each year. To determine the number of landslides occurring within areas of a single stand age over the period of record we need to go through year by year, find the weighted area in each stand age each year, and count the number of landslides associated with each stand-age increment each year:

$$\rho_{AGEj} = \frac{(N_{LS})_{AGEj}}{\sum_{iyr}^{nyr} \sum_{i}^{n_j} (aw_{Ti})} \tag{8}$$

The denominator now reflects the weighted areas in the jth stand age summed over each of the nyr years spanned by the inventory, the set of n_j DEM cells is different for each stand-age class each year, and the resulting density reflects the cumulative summed area repeated over each year of the inventory. Multiplying density by the number of years will give the density for the average area in that stand type over the period of record.

Variability year to year

Cutting of each harvest unit initiates a new stand age patch that then progresses, year by year, from age zero though progressively older ages. At any time, older patches have experienced a longer sequence of storms than younger patches, so each stand age has sampled a different set of storms. When we apply Equation (8) over multiple years of record, some of those years will have storms that triggered many landslides, hundreds in the case for Prince of Wales Island, and other years have no landslides at all. The juxtaposition of temporally varying stand-age distributions with temporally varying landslide numbers per year biases estimates of landslide density associated with each stand age. Stand-age classes

occupying larger areas than other stand-age classes in years with many landslides will have calculated landslide densities biased toward larger values.

We can adjust for this temporal variability by defining a temporal weighting term. In anticipation of future analyses, I'll call this a precipitation weighting, because large numbers of landslides are associated with large storms, so I suspect that we can define this weighting as a function of cumulative rainfall depth over some to-be-determined duration. For now, consider that we can parse the total number of landslides observed into those that occurred each year: $N_{LS} = \sum_{iyr}^{nyr}(N_{LS})_{iyr}$, where $(N_{LS})_{iyr}$ is the number of landslides observed in year iyr and the sum is over all nyr years in the period of record. If we look at the mean landslide density observed over the study area for a single year, following Equation (3), we can define a weighting term w_{Piyr} for each year as:

$$w_{Piyr} = \frac{\rho_{iyr}}{\rho_0}$$

Here $\rho_{iyr} = (N_{LS})_{iyr}/A$ and $\rho_0 = N_{LS}/A$, where A is the area of analysis, so w_P is defined simply as

the proportion of the total number of landslides occurring that year:

$$w_{Piyr} = \frac{(N_{LS})_{iyr}}{N_{LS}} \tag{9}$$

We can now rewrite Equation (5) as

$$N_{LS} = \sum_{iyr}^{nyr}\sum_{i}^{n}(aw_{Piyr}w_{Ti})\rho_{AGEi} \tag{10}$$

For a single stand-age class we can now write Equation (7) as

$$\rho_{AGEj} = \frac{(N_{LS})_{AGEj}}{\sum_{iyr}^{nyr}\sum_{i}^{n_j}(aw_{Piyr}w_{Ti})} \tag{11}$$

This gives the density associated with age-class j over the period of record adjusted for both variability in the terrain within different age classes and differences in the proportion of all landslides in each age class each year.

Soils

We can apply the same weighting strategy to look at landslide density for mapped soil types, adjusting for differences in topography and stand age across different soils.

As with topography in Equation (3), we can define a weighting function for stand age

$$w_{AGEi} = \frac{\rho_{AGEi}}{\rho_0} \tag{12}$$

and following Equation (4):

$$N_{LS} = \rho_0 \sum_{i}^{n}(aw_{Ti}w_{AGEi}) \tag{13}$$

6

Because w_{AGE} was defined using topographically weighted area, the mean value of $w_{Ti}w_{AGEi}$ over all n cells is still one.

Again, as with Equation (5)

$$N_{LS} = \sum_{iyr}^{nry} \sum_{i}^{n} \left(aw_{Piyr}w_{Ti}w_{AGEi}\right)\rho_{SOILi} \tag{14}$$

where ρ_{SOILi} is the landslide density associated with the soil type in the ith DEM cell. Parsing landslides and area (DEM cells) by soil type, as with Equation (7), we can define the landslide density for soil type j as:

$$\rho_{SOILj} = \frac{(N_{LS})_{SOILj}}{\sum_{iyr}^{nyr} \sum_{i}^{n_j} \left(aw_{Piyr}w_{Ti}w_{AGEi}\right)} \tag{15}$$

The density observed as a function of topography may also be affected by the spatial distribution of stand ages and soil types: if harvests or certain soil types are concentrated on lower-gradient terrain, then the effects of stand age and soil type will differ between this lower-gradient and higher-gradient areas. We can account for that in the same way: use weights determined for stand age and soil type to adjust the area used to calculate landslide density as a function of topographic index. An iterative approach is thus needed to fully implement these methods.

These methods are based on the concept of likelihood ratio (Chung, 2006), which is widely used for landslide susceptibility analyses (e.g., Strauch et al., 2019), although I have not seen it applied to address correlations among independent variables as done here. Use of likelihood ratio appeals to me because it uses all available data. Other methods, such as regression (Buma and Johnson, 2015) or machine learning (Goetz et al., 2015; Liu et al., 2020) can also be used to quantitatively rank locations in terms of landslide initiation potential and can more effectively deal with a larger number of independent variables. However, those methods all require sub-sampling of the DEM, which could result in sampling bias. Both likelihood ratio and machine learning approaches assume no *a priori* type of relationships between the dependent and independent variables, whereas regression models impose a certain type of relationship, e.g., that the variables are linearly related. Likelihood ratio and regression both provide a clear basis for ranking independent variables in terms of their apparent influence on the dependent variable: the ratio of observed frequency distributions in the first case and coefficient values in the second. Machine learning techniques provide little insight as to why relationships might arise: data goes in, numbers come out, but the details of how the input data produced those numbers is lost.

Topographic index

I described earlier how slope gradient could be used as an indicator of a relationship between topography and landslide density. Gradient is a good choice because many studies, both empirical and theoretical, demonstrate a distinct relationship between landslide potential and gradient. Conceptual models of how shallow landslides are triggered point to another potentially important feature of the topography: the area contributing infiltrating water that feeds subsurface flow during a storm or snow-melt event (e.g., Iverson, 2000). Failure potential increases with the depth of saturated flow; that depth is dependent on the amount of water flowing through the soil and the degree to which downslope flow directions converge. The amount of water increases as the upslope area contributing subsurface flow

increases; the degree of flow convergence can be estimated by the amount of curvature of contours across the slope (calculated as plan curvature). Physical models for shallow landsliding thus include specific contributing area (contributing area divided by contour length) as a parameter (e.g., Montgomery and Dietrich, 1994; Pack et al., 1998). However, water flows through soil at a limited rate, so storms that trigger landslides may not be of sufficient duration for the failure site to receive flow from the entire potential upslope contributing area. Hence, some researchers propose that partial contributing area, representing the upslope area that might actually be the source of infiltrating water during a storm, is a more appropriate parameter (Borga et al., 2002).

The physics of water infiltration and movement through soil are complex and models that seek to precisely represent these processes require information about soil properties that are generally unknown over regional scales. However, certain simplifications may provide sufficiently precise estimates of water fluxes to serve our needs. The kinematic wave approximation is widely used to estimate flow velocities, with which we can approximate the rate of subsurface flow using the Darcy velocity: $v = K \sin \theta$, where v is flow velocity, K is saturated hydraulic conductivity of the soil, and θ is the direction of flow relative to horizontal. For shallow soils, flow direction θ is generally equated with ground-surface gradient (e.g., Montgomery and Dietrich, 1994; note however objections by Iverson, 2000). Using surface gradient estimated from the DEM, we can then trace flow paths upslope to delineate the area potentially contributing flow to each DEM cell within a specified duration. In the past, computing power was insufficient for this task, so less computationally intensive methods were proposed (Chirico et al., 2003), but we can now explicitly delineate contributing area for each DEM cell for a specified storm duration. We use the D-infinity flow-direction algorithm for this task (Tarboton, 1997).

For the Sitka landslide susceptibility analysis, I used plan curvature multiplied by gradient as the topographic index. Plan curvature addresses the degree of topographic convergence for subsurface flow, but that index did not address contributing area. For this analysis, I use slope gradient multiplied by partial contributing area. This provides an index tied more directly to the processes triggering shallow landslides.

On the ground, topographic attributes like gradient are measured over specific length scales. On uneven terrain, the gradient measured over two meters will not match that measured over ten. A length scale must therefore be chosen for calculation of topographic attributes from a DEM. The lower limit of this length scale is governed by the horizontal resolution of the DEM. I am using Lidar-derived DEMs sampled at a 2-meter resolution, so the smallest topographic features that can potentially be resolved extend for at least 4 meters. The ground surface exhibits topographic features spanning a great range of length scales; we want to identify those features appropriate for the processes driving shallow landsliding. The DEMs may also exhibit a certain amount of noise: we want to choose a length scale that won't be overly influenced by noise in the DEM. Frankly, I don't know what the best length scales are. The narrowest mapped landslide scars in the inventory extend laterally about 5 meters. This is consistent with field-measured values reported by Johnson et al. (2000) for landslides on Prince of Wales Island triggered by a large storm in 1993. I suspect, however, that groundwater flow paths respond to topography over a longer length scale and a 5-meter round bump or divot is not generally a controlling factor. I calculated gradient and flow accumulation using flow directions calculated for a DEM smoothed over a 15-meter length.

Landslide initiation points

Mapped landslide polygons show where landslide scars were observed in aerial photographs. The zone where a landslide initiated is within its polygon (assuming the polygon boundaries are accurately located), but the precise location and extent is uncertain. The Tongass National Forest landslide inventory includes both polygons delineating the visible landslide scar and points indicating the initiation point estimated by the photo interpreter. For the Sitka analysis, I chose the least-stable point within the upper portion of each polygon. I'll use the same strategy here, but also use the initiation points from the inventory and compare the results.

From the Tongass landslide inventory geodatabase, I selected polygon records with recorded landslide types (field FAIL_TYPE) of SOAR-DEAV-FLOW, SOAR-DEFL-FLOW, and TRZO-DEFL-FLOW. From these, road-associated landslides (field RD_RELATED = Y) were removed.

Analysis Area

The shaded relief image in Figure 1 shows the portion of Prince of Wales Island for which the Lidar DEM was available. This area covers 5,657 km^2 and the landslide inventory includes 2179 non-road-related landslides of the types listed above.

Results

Topographic index

An example of calculated gradient, partial contributing area, and the resulting topographic index is shown in Figure 2. The valley walls contain extremely steep terrain, with gradients exceeding 100%. The partial contributing area is greater in areas with steeper gradients and topographic convergence. I chose a short duration for calculating partial contributing area, 5 hours (with an applied saturated hydraulic conductivity of 5m/hr), to highlight the small bedrock hollows present in many of the upper slopes. The topographic index, calculated as the product of gradient and partial contributing area, thus emphasizes steep slopes and convergent topography.

Initiation points are shown in Figure 3 for the manually digitized points from the inventory and those automatically placed at the maximum index value within the upper portion of the landslide polygon. The offset between the two ranges from a few meters to a few tens of meters.

Landslide density as a function of topographic index

Figure 4 shows the cumulative distribution of topographic index values over the analysis area (excluding areas with slope gradient less than 40%) and for the inventoried landslide initiation points. Curves for the manually digitized points from the inventory and from those automatically placed at the maximum index values in the upper portions of the inventory polygons are both shown. The frequency distribution for landslides, whether based on the manually placed or automated points, both diverge substantially from the frequency distribution of index values over the analysis area. The landslide initiation points are not randomly distributed but tend to fall on higher index values.

Landslides were sorted into bins, with each bin containing the same number of landslides. The range of index values spanned by landslides in each bin was then used to determine the area associated with each bin. This provided the cumulative number of landslides and the associated cumulative area sorted by index value for the specified number of bins. The slope of the resulting cumulative area versus

cumulative landslides at any index value indicates the number of landslides found within a small increment of area (dN_{LS}/dA) about that index value, which provides an estimate of landslide density for each index value as illustrated in Figure 5 for the maximum-index-value initiation points. Low-index-value bins contain a lot of area for the set number of landslides, so the slope (landslide density) is low. High-index-value bins contain very little area for the same number of landslides, so the slope is large. The associated topographic weighting functions are then found by dividing the density at each index value by the mean landslide density over the analysis area.

As seen in Figure 4, the manually placed points fall at lower index values. Figure 6 shows how the inferred topographic weighting differs for the two sets of initiation points. For the manually digitized points, weighting is larger at low index values and lower at high index values compared to weights obtained from the automatically placed points. Recall that the weight indicates how landslide density at a particular index value compares to the average density over the entire area of analysis. The area-averaged mean weight must equal one, so a shift to larger weights at lower index values requires a shift to lower weights at large index values.

The maps in Figure 7 show the spatial distribution of modeled weight values obtained using both the automated and manual placement of landslide initiation points for a small portion of the study area. The patterns are similar, since they are based on the same spatial distribution of topographic index values, but the contrast in weighting values is much larger for weights obtained using the automatically placed points.

Variations of landslide density with stand age

The activity polygon GIS coverage for the Tongass National Forest provides harvest-unit boundaries and harvest dates, shown in Figure 8 for the area examined in previous figures. These GIS records can be used to map the spatial distribution of stand ages each year over the period of record. Figure 9 shows the amount of harvest within the study area over time in the upper graph and the number of landslides observed each year in the lower graph. The number of landslides varies dramatically from year to year, with many years experiencing no landslides, and in any year with landslides (post 1960)[2], the proportion of landslides occurring within harvest units is larger than the cumulative proportion of the study area harvested in any year.

The landslide analysis excludes terrain with a gradient less than that (40%) within which no landslide initiation points are located. This steeper, potentially unstable terrain includes 1604 km^2 out of the total 5655 km^2 study area. As of 2019, harvest units cover 226 km^2 of the potentially unstable area. Looking solely at harvested areas and never-harvested areas within the potentially unstable terrain we find a landslide density of 2.70/km^2 within harvested areas and 1.12/km^2 outside harvested areas: an increase of 2.4 times in harvested areas. This is consistent with increases observed in other studies.

Note, however, that for the period during which landslides in this inventory occurred, the area in harvest units was typically much less than 226 km^2 (Figure 11). When the timing of harvests and

---

[2] The number of landslides recorded for 1948 and 1960 may represent a cumulative sum over previous years, reflecting the availability of historical aerial photos. For many of these, the year of occurrence was recorded as a negative value: I counted all of these as occurring prior to harvest in the initiation location.

landslides is accounted for, we find a density of 6.29/km^2 in harvested areas and 1.02/km^2 in areas not previously harvested: an increase of 6.2 times in harvested areas.

We also find that areas harvested are generally located in slightly more stable terrain than areas never or not previously harvested. The effect of this difference on inferred landslide density depends on the magnitude of the topographic weighting found in the two zones. As we saw in the last section, the magnitude of topographic weighting can vary depending on the method used to identify landslide-initiation locations. Using a topographic weight function derived from the automated point placement, the red smoothed line in Figure 6, the average weight for harvested areas is 0.57, indicating that without harvest, landslide density in these zones would be a bit more than half that of the average over the entire analysis area, not the large increase that we observed. The average weight in areas never or not yet harvested is 1.07, indicating a landslide density in these areas slightly greater than the average. Using topographic weighting derived using the manually digitized points from the inventory (the blue smoothed line in Figure 6) the average weight for harvested areas is 0.75 and for unharvested areas 1.04. Both results indicate that, within the potentially unstable analysis area (gradient > 40%), harvest units generally lie on more stable terrain. To identify changes in landslide density associated with timber harvest, we need to account for this difference in topography between harvested and not-harvested zones.

Another potentially confounding factor is the large difference in the number of landslides from year to year. From Figure 9 we see that, since extensive harvesting commenced after 1959, a large proportion of landslides in the inventory occurred in just three years: 1988, 1993, and 2001. Figure 10 shows the distribution of harvested area by stand age for those years. Assuming that differences in the number of landslides year to year reflects differences in storm characteristics year to year, the impact of any single storm is not equally distributed across stand ages. In 1988, for example, stand age 22 years encompassed a little more than 14 km^2 whereas stand age 8 encompassed only 2 km^2. Over the period of record, this might bias our estimate of landslide density for stand age 22 to larger values. I used the "precipitation weighting" factor, w_P from Equation (9), to reduce this bias.

Landslide numbers year to year provide the precipitation weighting factor for each year. Using the activity polygons, I mapped stand age year by year and overlaid the landslides that occurred each year. With the topographic weighting functions determined as described previously, I then calculated the weighted area ($aw_{Piyr}w_T$) year by year for Equation (11). Accounting for both landslide numbers year to year and differences in topography of the terrain covered by harvested and not-harvested areas year by year, I find an average landslide density in harvest units of 11.53/km^2 and in not-harvested areas of 1.05/km^2 using topographic weighting derived with automatic initiation point placement, and 8.74/km^2 in harvest units versus 1.02/km^2 in not-harvested areas using topographic weighting derived from the manual initiation point placement. These results indicate an overall increase in landslide density in harvested areas of 8.6 to 11 times. This is the average over all stand ages. We can also look at how landslide density varies with stand age.

The variation of landslide density with stand age can be estimated using the relationship between cumulative weighted area and cumulative number of landslides, plotted in Figure 11. The slope of the curve defined by these points gives the density by stand age as defined in Equation (11). Three zones are evident in the graph: a zone of steep gradient (high density) extending to stand ages of about 10 to 15 years (shown by the small numbers at each point); a zone of lower gradient from about 15 to 35 years,

and a much lower-gradient zone extending to higher stand ages. The first derivative of a smooth curve fit through these points gives an estimate of landslide density; dividing that value by the mean density for the study area gives a weight for each stand age, shown in Figure 12 for both automatic and manual initiation-point placement. These results indicate high densities post harvest, 15 to 20 times the average over the study area, that decrease over the next two decades and then level off at about 4 to 5 times the average between 20 and 30 years stand age. Densities then drop to match the background density observed in unharvested areas at about 55 to 60 years stand age.

Landslide density for mapped soil types

I used digital soil surveys for the Tongass National Forest[3] to delineate different soil types (Figure 13). I do not have information on the scale or mapping protocols used. The smallest delineated units within the study area cover about 5 acres. Landslide densities for each soil type are calculated using Equation (15), which accounts for differences in topography and stand age across different soil units. Not all soil units were included in the analysis area, which excluded terrain with gradient less than 40%, and not all soil units within the analysis area contained landslide initiation points. For soil types that contained landslide initiation points, Figure 14 shows the area and number of landslides in each. Some of these involve little area and few landslides. In applying Equation (15), I excluded soil types with five or fewer landslides and with area less than six km^2. The resulting weights (density for each unit divided by the mean density over the analysis area) are shown in Figure 15.

Topographic setting is a factor in delineating soil types. This is manifest by the variation in mean topographic weighting found within each soil type, also shown in Figure 15. The number of landslides observed in a particular soil type is a function of both the propensity of the soil to fail, indicated by the relative weights in Figure 15, and where it lies in the landscape, reflected in variation in topographic weight.

Figure 15 also shows how topographic weighting differs between harvested and not-harvested areas within each soil type. Within each soil type, areas harvested lie on more stable terrain than areas that had not been harvested.

Landslide Rate

An estimate of background landslide rate, that is, the rate that would have occurred in the absence of timber harvest over the period of observation, is provided using the topographic and soil-type weight at each DEM cell multiplied by the mean landslide density and divided by the number of observation years (91). Inferred rates are shown in Figure 16 obtained using weighting values inferred using both the manual and automated landslide initiation point placement.

Discussion

Proportion of sites as a measure of susceptibility

Uncertainty in how to relate landslide initiation location to topographic attributes can result in a substantial difference in the landslide rate inferred at any specific point. The average rate over the study area is the same in each case, but values differ point to point. Automated placement of initiation points at the highest topographic index value within the upper portion of the landslide polygons produces

---

[3] https://gis.data.alaska.gov/datasets/f5c457ee784d4ccc871f8c2d8cb02780

greater contrast in topographic weighting than obtained with manual placement based on aerial photo interpretation. Automated placement gives bigger high values and smaller low values, as shown in Figure 6. When modeled rates are mapped to the ground as shown in Figure 16, automated placement produces more spatially concentrated high values but also a greater extent of low values than found with rates inferred using manual initiation point placement.

Is one better than the other? Based on the spatial distribution of inferred rates, a graph showing the proportion of mapped landslides versus the proportion of area shows that automated placement encompasses a greater proportion of landslide initiation points with less area than manual placement, as shown in Figure 17. But that is an artifact of the process used to locate initiation points; it is not a test of which method is better. In fact, as landslide occurrences are monitored into the future and new landslide polygons and initiation points added to the inventory, when these are used to verify these model results, we would find that both methods predict landslide locations equally well.

Another way to view these results is to map zones in terms of the proportion of landslides that have occurred. Then the range of values is the same for each case, from zero to one, as shown in Figure 17. These proportions are shown in the maps of Figure 18. Each color indicates the area containing 20% of the landslide initiation points, starting with the least-stable (highest-density, dark red) zones. The dark red zones contain 20% of all mapped points; the dark red and orange zones combined contain 40%; all colors combined contain all mapped points. With automated point placement, points are concentrated in higher topographic-index zones, so the least stable (highest rate) 20% of points fall within a smaller area than with manual placement. Likewise, the most stable (lowest rate) 20% of points fall within a larger area with automated placement.

Inconsistencies in landslide polygon placementfi

As we have seen, the apparent resolution of unstable zones depends on the method used to determine initiation-point locations. Errors in georeferencing of landslide polygons add to this uncertainty. An example is shown in Figure 19. Compared to the DEM, the landslide polygons and associated initiation points appear to be displaced to the east about 20 to 30 meters. This results in the initiation points landing on zones with a lower topographic index than the more probable location to the west. Landslide headscarps are as narrow as 5 meters; the Lidar DEM can resolve topographic features of the same extent. A displacement of ten or more meters can entirely miss the actual initiation zone. The scale of photos varies with location in the photo, so the photos must be orthorectified to a consistent scale and coordinate system. Orthorectification requires a terrain model, which serves as a basemap to which features are aligned. The Lidar DEM would provide a terrain model with high resolution and precision, but it was not available when the photos were used to determine landslide polygon locations, so it is probably inevitable that there are discrepancies between polygon position and landslide locations on the DEM. If displacements are systematic and consistent, e.g., all polygons are displaced 23 m east, we can shift them, but the apparent displacement is not consistent.

To deal with this potential error, initiation points may be moved from their digitized location to the likely least stable point within a specified radius, e.g., to the point with steepest gradient. I have done something similar here by placing the initiation point at the DEM cell with largest topographic index found within the upper portion of each landslide polygon.

If it is assumed that polygon locations should align with topographic features, e.g., that runout tracks should be aligned with swales or channels visible in the DEM, we could potentially use those features to shift individual polygons. This will bias results to the topographic features we chose, just as here automated initiation point placement biased results to zones with larger topographic index values. This bias is not wrong, however, if these are the topographic features where landslides occurred. This may be a strategy worth evaluating.

Spatial extent of landslide failure zones versus DEM cell size

To compare the distribution of topographic index values between landslide sites and the terrain overall, I have associated each landslide initiation point to a single DEM cell. This provides a single index value for each landslide, but also presents a discrepancy in scale. The DEM used was sampled to a 2-m point spacing whereas landslide head scarps may be five to fifty meters wide (Johnson et al., 2000). I have addressed this by calculating topographic attributes over a scale of 15 meters. Another complementary approach would be to assign each DEM cell the mean or maximum index value found within a radius representative of a typical landslide initiation zone (i.e., a focal maximum or focal mean). Does landslide initiation respond to topographic features at the meter scale, the 5-meter scale, the 10-meter scale? If head scarps are indicative of that scale, then something in the range of 5 to 10 meters may be appropriate.

Using a focal maximum or focal mean to represent topographic controls on landslide initiation will tend to reduce the contrast in modeled landslide density between high and low susceptibility areas similarly to the way that manual point placement did relative to automated point placement.

Lidar DEM shows post-landslide topography

How different is post landslide topography from pre-landslide topography? How much does this affect the resulting topographic index? We find that landslides are located preferentially in locations with topographic convergence – swales and hollows – but to what extent are the swales and hollows we measure formed by the last landslide? Ideally, we would have multiple Lidar data sets with landslides that occur between the collection dates. We do not have that, yet. It may be worthwhile to do some sensitivity analysis to see how much these techniques respond to filling in of observed landslide initiation sites. I have not done that. However, note that the topographic index used here is sensitive to upslope conditions via the partial contributing area term, which have not been affected by prior landsliding, and to slope gradient measured over a 15-m length. Johnson et al. (2000) report soil depths for landslides on Prince of Wales Island of 0.4 to 2.2 meters, with a mean of about 1.2m. Over a 15-m length, a 1.2m loss of soil translates to an 8% increase in slope; a 2.2m loss to a 15% increase in slope.

Variations in land cover other than stand age

This analysis indicates that change in land cover associated with timber harvest have a large transient effect on landslide rate. Clearly, changes in land cover are important. In this analysis, the only attributes of land cover examined are whether or not timber harvest has occurred, and if it has, the time since harvest when landslides are observed. I have not examined how other aspects of land cover might be associated with variations in landslide density. Such analysis is hindered by the need to examine land cover at the time each landslide occurs. The inventory involves landslides spanning 91 years. The activity database allowed me to map the distribution of harvested versus not harvested zones and to map the stand age of each harvest unit each year over that interval. I do not have similar temporal data for other cover attributes. The Lidar point cloud, for example, provides a variety of potentially useful measures:

vegetation height and volume density, for example, but for one point in time. If there are attributes that do not change over time, these might be worth examining. For example, if vegetation height in non-harvest zones is mostly constant over the period of the inventory, then we may be able to use that to look for variations in landslide density in non-harvest zones with vegetation height.

Detection bias in photo surveys

With aerial photos it can be difficult to see small landslides, so it is inevitable that some landslides are missed and not counted. Landslides under forest canopy are more difficult to see than landslides in clear cuts, so the proportion of landslides missed may be greater in forested areas. Comparison of field- and photo-based inventories indicate that the proportion missed can be substantial (Brardinoni et al., 2003) and varies with landslide size and stand age (Miller and Burnett, 2007). Some of the variation in landslide density with stand age observed in this analysis of the Tongass data may originate from bias in the proportion of landslides visible in aerial photos under forest stands of different age. Miller and Burnett (2007) used the distribution of mapped landslide sizes to estimate the proportion of landslides missed under different forest-cover classes. A similar analysis could be done here, but would be confounded if landslide sizes tend to vary with stand characteristics. Johnson et al. (2000) found in field surveys of 45 landslides on Prince of Wales Island following a large storm in 1993 that landslides in old growth forests tended to be larger in aerial extent than landslides in other forest types. For now, the effect of possible detection bias on this analysis is unknown.

Uncertainties associated with area examined

In this analysis, I examined topographic zones (based on topographic index) of variable size, land cover types (based on time since harvest) of variable size, and soil-inventory polygons of variable size. How does the size of the area examined influence confidence in results? I'll use a simple conceptual model to illustrate how area examined affects confidence in the result.

Consider a study area of several thousand square kilometers, as we have here. Imagine that the terrain is homogenous with topographic, land cover, and soil-type influences on landsliding that are uniform across the study area. If our landslide inventory produces a density of $1/km^2$ for the study area, how many landslides are we likely to see if we look at smaller areas of 10 km^2, or 5 km^2, or 1 km^2? If landslide locations are randomly located within any zone of uniform density and the presence of a landslide at one point does not alter the probability of seeing a landslide in any neighboring point, then the probability of finding a landslide, or any specified number of landslides, within a fixed area can be estimated with the Poisson distribution[4] as

$$P(k) = \frac{(\rho A)^k e^{-\rho A}}{k!}$$ (16)

where $P(k)$ is the probability of finding k landslides within area A, ρ is the average landslide density over area A, e is the base of the natural logarithm, and $k!$ indicates the factorial of k. For a specified density, Equation (16) can be used to estimate confidence intervals showing how much observed densities might vary with the area examined, as shown in Figure 20. The smaller the area, the greater the range of landslide densities we might encounter. For average densities on the order of that observed here ($1/km^2$), there is an inflection in the confidence intervals around 10 km^2 with uncertainty decreasing at a slower rate for areas larger than that. An examination of Figure 10 shows that the area in any single stand age in any year is typically much smaller than 10km^2. However, the distribution of

---

[4] https://en.wikipedia.org/wiki/Poisson_distribution

stand ages was mapped for every year over the 91-year period of record, so the cumulative area examined over time is considerable larger. However, even over this time span, the cumulative area in stands of age greater than 60 years is less than 10 km^2. Hence, I only included stand ages up to 60 years in that analysis. The cumulative area in each soil type polygon is shown in Figure 14. Soil type TOK at 6 km^2 is the only soil type with any landslides that encompassed less than 10 km^2, so I did include it in the analysis but recognizing that there is substantial uncertainty in the weight value estimated for that soil type.

Topographic Index

I have not yet compared the choice of topographic index used here against other options. I have used other indices in other studies. For landslide assessments in Washington State I've used a factor-of-safety-based index (Miller, 2004)[5] and a gradient times convergence index (Miller, 2008)[6], with convergence calculated as the contour length crossed by flow exiting a DEM cell. In Oregon, Kelly Burnett and I (Miller and Burnett, 2007) used the topographic relationship from the SHALSTAB model (Dietrich et al., 1998; Montgomery and Dietrich, 1994). For the Sitka landslide susceptibility analysis (Miller, 2019)[7] I used slope times plan curvature, which is similar to the slope times convergence. This is the first use of partial contributing area as a component of the topographic index. Each iteration of the index is, I think, an improvement on the previous, but the options should be compared. Comparisons can be made using the proportion-of-area versus proportion-of-landslides curves. For such comparisons, the same method of choosing initiation points must be used for each case.

In Southeast Alaska, landslides are also triggered by strong winds. Estimated wind exposure is a function of local topography and can be incorporated into landslide susceptibility assessments (Buma and Johnson, 2015). Indices including a measure of wind exposure should also be evaluated.

Assumptions in this analysis

In implementing the concept of likelihood ratio in this analysis, I have not yet fully incorporated potential interactions among the effects of topography, stand age, soil type, and storm magnitude on landslide density. The shape of the function relating topographic index and landslide density, like that shown in Figure 6, is assumed unchanged for different stand ages, soil types, and storms: the magnitude increases or decreases with the weighting assigned for each stand age (w_{AGE}), soil type (w_S), and analysis year (w_P), but the shape of the relationship stays the same. If a topographic index of 8 has twice the landslide density as a topographic index of 6, this remains the same under all stand ages, all soil types, and all years. This seems like a reasonable assumption to enable this analysis, but I do not know how well it applies. It could be that timber harvest increases the potential for landsliding more for low-gradient areas than for high-gradient areas (Brardinoni et al., 2002), for example, in which case, this analysis would underestimate the increase in landslide density associated with harvest. Or it could be the other way around. With this large dataset, particularly as we expand analysis to include other areas covered by the Tongass Landslide inventory, I think we will be able to address this issue.

---

[5] http://citeseerx.ist.psu.edu/viewdoc/download?doi=10.1.1.660.4824&rep=rep1&type=pdf
[6] http://www.nwwatershed.org/uploads/pdf/MillerReport2008.pdf
[7] https://terrainworks.sharefile.com/share/view/s811f9d15401149f6993540d2798928c8

Climate

Variability in the number of landslides year by year points to a primary relationship between storm characteristics and landslide rate. It may be feasible to relate the number of landslides observed in any year to some measure of the storm magnitude that triggered those landslides (Reid, 1998; Reid and Page, 2002). I did not seek precipitation data to evaluate this, but it may be worth examining. If a relationship is found, then landslide rate can be described as a function of storm regime. If changes in storm regime associated with climate change can be anticipated, such an analysis provides a means of anticipating climate-change impacts on landslide frequency.

How should landslide initiation locations be determined for assessment of susceptibility?

This analysis shows that choice of method for placing landslide initiation locations on the DEM has a large influence on the resulting determination of topographic associations with landslide density. Because the same method will be used for model calibration and validation, any method can prove to be highly accurate in terms of the resulting model's ability to predict the zone where a given proportion of landslides was observed or will occur. The difference is in the size of those zones. Methods that choose the least-stable point within some constrained area – the upper portion of a landslide polygon for example – will result in smaller high-susceptibility zones and larger low-susceptibility zones. The degree of contrast between high- and low-susceptibility terrain as expressed with the proportion-of-area versus proportion-of-landslides curve can serve as a measure of model "success", but I don't know if it is an appropriate measure.

In doing this analysis, I've come to think we need to better assess the spatial scale over which soil failure occurs and target our analyses to that scale. With Lidar, we can now see the topographic features associated with shallow landsliding, but we are also seeing features that are smaller than a shallow landslide failure zone. What is the appropriate length for characterizing topographic controls on landslide processes? This is a choice we need to make a priori; as I mentioned above, we cannot test it empirically because calibration and validation both use the same length scales. Having chosen a length scale, then we can use area versus landslide curves and other measures to assess different topographic indices and methods for initiation-point placement. In the meantime, the results of this analysis provide a first iteration for spatially distributed assessment of shallow landslide initiation susceptibility.
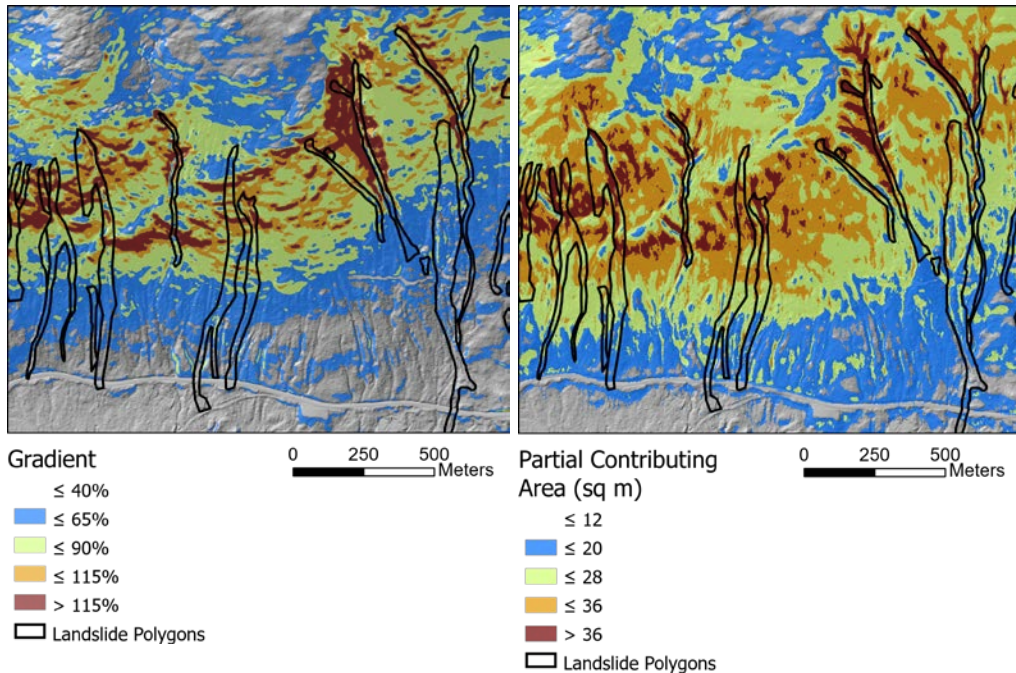
Amaranthus, M. P., Rice, R. M., Barr, N. R., and Ziemer, R. R., 1985, Logging and forest roads related to increased debris slides in southwestern Oregon: Journal of Forestry, v. 83, no. 4, p. 229-233.

Borga, M., Fontana, G. D., and Cazorzi, F., 2002, Analysis of topographic and climatic control on rainfall-triggered shallow landsliding using a quasi-dynamic wetness index: Journal of Hydrology, v. 268, p. 56-71.

Brardinoni, F., Hassan, M. A., and Slaymaker, O. H., 2002, Complex mass wasting response of drainage basins to forest management in coastal British Columbia: Geomorphology, v. 49, p. 109-124.

Brardinoni, F., Slaymaker, O., and Hassan, M. A., 2003, Landslide inventory in a rugged forested watershed: a comparison between air-photo and field survey data: Geomorphology, v. 54, p. 179-196.

Buma, B., and Johnson, A. C., 2015, The role of windstorm exposure and yellow cedar decline on landslide susceptibility in southeast Alaskan temperate rainforests: Geomorphology, v. 228, p. 504-511.

Chirico, G. B., Grayson, R. B., and Western, A. W., 2003, On the computation of the quasi-dynamic wetness index with multiple-flow-direction algorithms: Water Resources Research, v. 39, no. 5.

Chung, C.-J., 2006, Using likelihood ratio functions for modeling the conditional probability of occurrence of future landslides for risk assessment: Computers & Geosciences, v. 32, no. 8, p. 1052-1068.

Dhakal, A. S., and Sidle, R. C., 2003, Long-term modelling of landslides for different forest management practices: Earth Surface Processes and Landforms, v. 28, no. 8, p. 853-868.

Dietrich, W. E., de Asua, R. R., Coyle, J., Orr, B., and Trso, M., 1998, A validation study of the shallow slope stability model, SHALSTAB, in forested lands of Northern California: Stillwater Ecosystem, Watershed & Riverine Sciences.

Goetz, J. N., Brenning, A., Petschko, H., and Leopold, P., 2015, Evaluating machine learning and statistical prediction techniques for landslide susceptibility modeling: Computers & Geosciences, v. 81, p. 1-11.

Guthrie, R. H., 2002, The effects of logging on frequency and distribution of landslides in three watersheds on Vancouver Island, British Columbia: Geomorphology, v. 43, no. 3-4, p. 273-292.

Imaizumi, F., Sidle, R. C., and Kamei, R., 2008, Effects of forest harvesting on the occurrence of landslides and debris flows in steep terrain of central Japan: Earth Surface Processes and Landforms, v. 33, no. 6, p. 827-840.

Iverson, R. M., 2000, Landslide triggering by rain infiltration: Water Resources Research, v. 36, no. 7, p. 1897-1910.

Johnson, A., and Wilcock, P. R., 1998, Effect of root strength and soil saturation on hillslope stability in forests with natural cedar decline in headwater regions of SE Alaska, Headwaters: Water Resources and soil Conservation; Fourth International Conference on Headwater Control: Merano, Italy.

Johnson, A. C., Swanston, D. N., and McGee, K. E., 2000, Landslide initiation, runout, and deposition within clearcuts and old-growth forests of Alaska: Journal of the American Water Resources Association, v. 36, no. 1, p. 17-30.

Liu, Z., Gilbert, G., Cepeda, J. M., Lysdahl, A. O. K., Piciullo, L., Hefre, H., and Lacasse, S., 2020, Modelling of shallow landslides with machine learning algorithms: Geoscience Frontiers.

Miller, D., 2008, Landslide Hazard and Erosion Susceptibility Assessment. Tarboo-Dabob Bay, Washington: Northwest Watershed Institute.

Miller, D., 2019, Modeling susceptibility to landslides and debris flows in southeast Alaska: Terrainworks, Mt. Shasta, CA.

Miller, D. J., 2004, Landslide Hazards in the Stillaguamish Basin: A New Set of GIS Tools: The Stillaguamish Tribe of Indians.

Miller, D. J., and Burnett, K. M., 2007, Effects of forest cover, topography, and sampling extent on the measured density of shallow, translational landslides: Water Resources Research, v. 43, no. W03433.

Montgomery, D. R., and Dietrich, W. E., 1994, A physically based model for the topographic control on shallow landsliding: Water Resources Research, v. 30, no. 4, p. 1153-1171.

Pack, R. T., Tarboton, D. G., and Goodwin, C. N., 1998, The SINMAP approach to Terrain Stability Mapping, 8th Congress of the International Association of Engineering Geology: Vancouver, British Columbia, Canadia.

Reid, L. M., 1998, Calculation of average landslide frequency using climatic records: Water Resources Research, v. 34, no. 4, p. 869-877.

Reid, L. M., and Page, M. J., 2002, Magnitude and frequency of landsliding in a large New Zealand catchment: Geomorphology, v. 49, p. 71-88.

Schmidt, K. M., Roering, J. J., Stock, J. D., Dietrich, W. E., Montgomery, D. R., and Schaub, T., 2001, The variability of root cohesion as an influence on shallow landslide susceptibility in the Oregon Coast Range: Canadian Geotechnical Journal, v. 38, p. 995-1024.
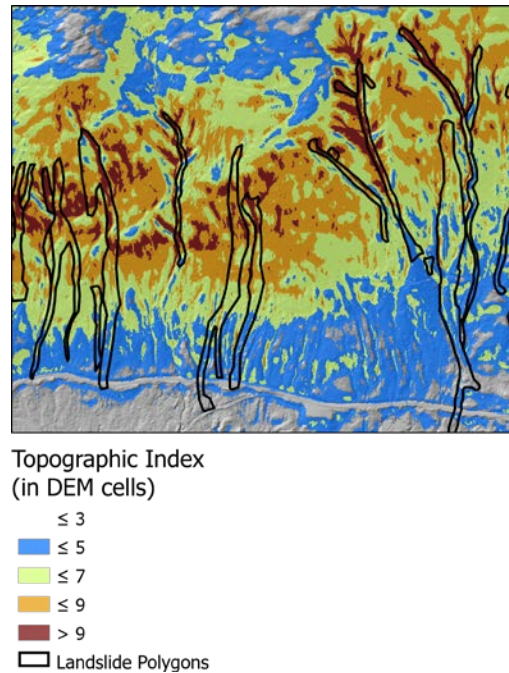
Sidle, R. C., 1992, A theoretical model of the effects of timber harvesting on slope stability: Water Resources Research, v. 28, p. 1897-1910.

Strauch, R., Istanbulluoglu, E., and Riedel, J., 2019, A new approach to mapping landslide hazards: a probabilistic integration of empirical and process-based models in the North Cascades of Washington, U.S.A: Natural Hazards and Earth System Sciences Discussions, p. 1-29.

Swanson, F. J., and Dyrness, C. T., 1975, Impact of clearcutting and road construction on soil erosion by landslides in the western Cascade Range, Oregon: Geology, v. 3, no. 7, p. 393-396.

Swanston, D. N., 1969, Mass wasting in coastal Alaska: USDA Forest Service.

-, 1997, Controlling stability characteristics of steep terrain with discussion of needed standardization for mass movement hazard indexing: a resource assessment: USDA Forest Service, Pacific Northwest Research Station.

Swanston, D. N., and Marion, D. A., 1991, Landslide response to timber harvest in Southeast Alaska, *in* Fan, S., Kuo, Y., ed., Fifth Federal Interagency Sedimentation Conference, Volume 2.

Tarboton, D. G., 1997, A new method for the determination of flow directions and upslope areas in grid digital elevation models: Water Resources Research, v. 33, no. 2, p. 309-319.

Wolfe, M. D., and Williams, J. W., 1986, Rates of landsliding as impacted by timber management activities in northwestern California: Bulletin of the Association of Engineering Geologists, v. 232, no. 1, p. 53-60.

Wu, T. H., and Swanston, D. N., 1980, Risk of landslides in shallow soils and its relation to clearcutting in southeastern Alaska: Forest Science, v. 26, no. 3, p. 495-510.

Ziemer, R. R., and Swanston, D. N., 1977, Root strength changes aftger logging in southeast Alaska: USDA Forest Service.
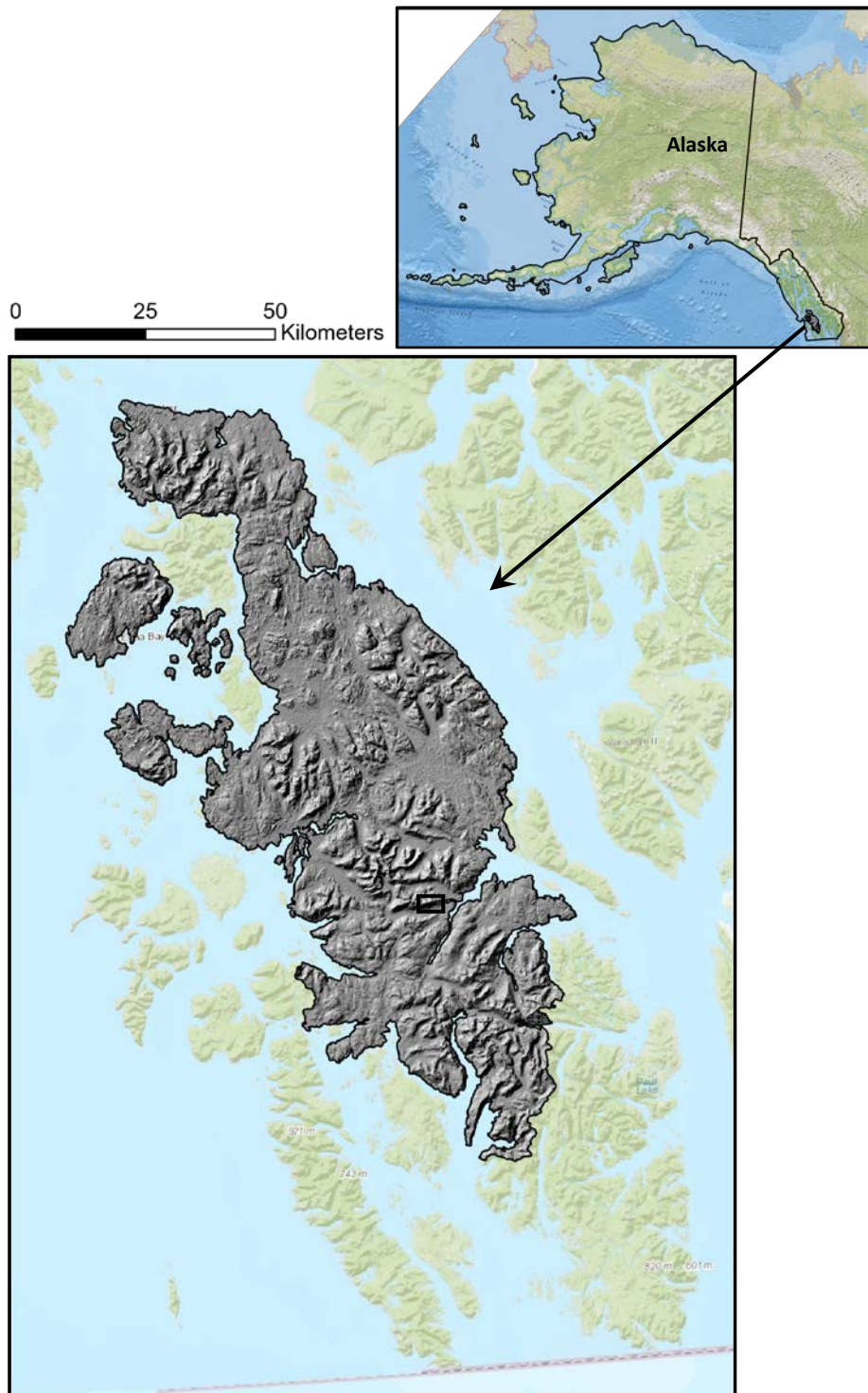
Figure 1. Prince of Wales Island. Shaded-relief image indicates the area included in this analysis. The black rectangle on the shaded relief image indicates the area shown in subsequent figures.
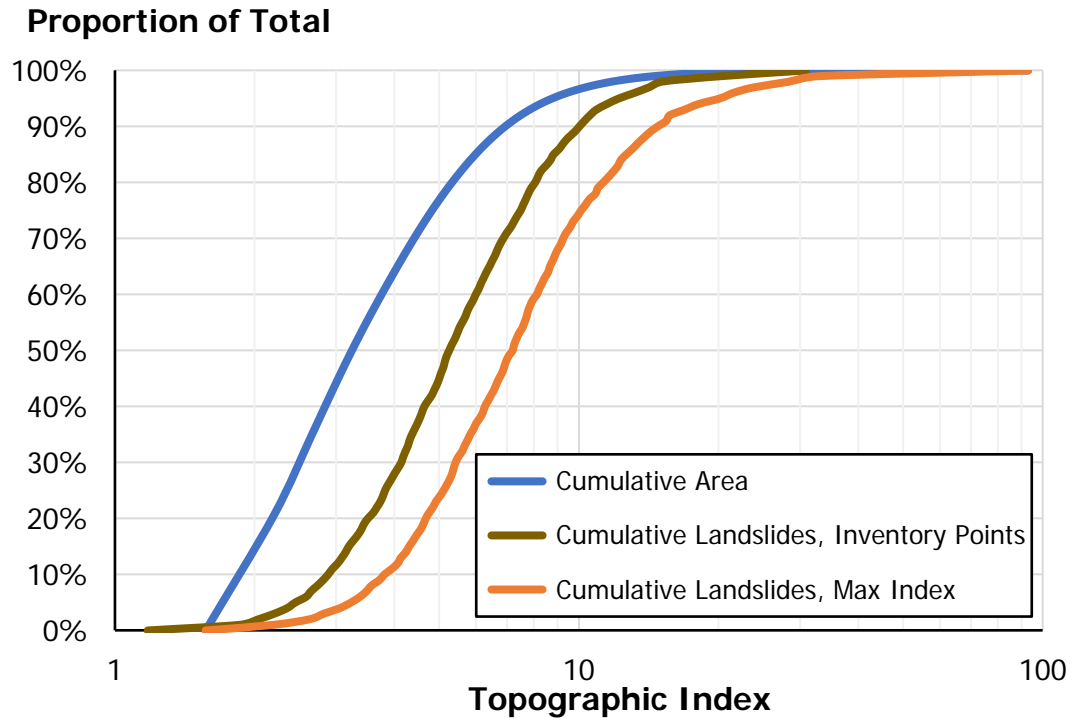
Gradient
- ≤ 40%
- ≤ 65%
- ≤ 90%
- ≤ 115%
- > 115%
- ☐ Landslide Polygons

0   250   500 Meters

Partial Contributing Area (sq m)
- ≤ 12
- ≤ 20
- ≤ 28
- ≤ 36
- > 36
- ☐ Landslide Polygons

0   250   500 Meters

Figure 2. The topographic index is derived from the product of slope gradient and partial contributing area. Slope gradient was calculated over a diameter of 15 meters; partial contributing area used the D-infinity flow-direction algorithm with DEM smoothing over 15 meters, a storm duration of 5 hours, and saturated hydraulic conductivity of 5m/hr. The resulting topographic index is shown at the right. All images include landslide polygons from the Tongass National Forest landslide inventory.

Topographic Index (in DEM cells)
- ≤ 3
- ≤ 5
- ≤ 7
- ≤ 9
- > 9
- ☐ Landslide Polygons

Topographic Index

- ≤ 5
- ≤ 7.5
- ≤ 10
- ≤ 12.5
- > 12.5

- ○ Inventory Initiation Points
- ● Maximum Index Initiation Points
- ☐ Landslide Polygons

0   250   500 Meters
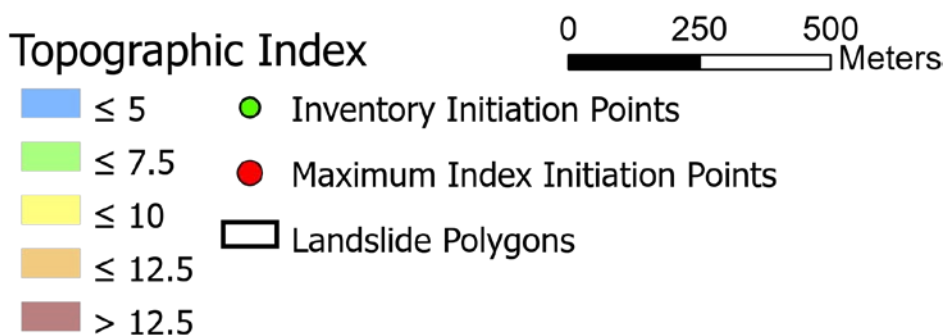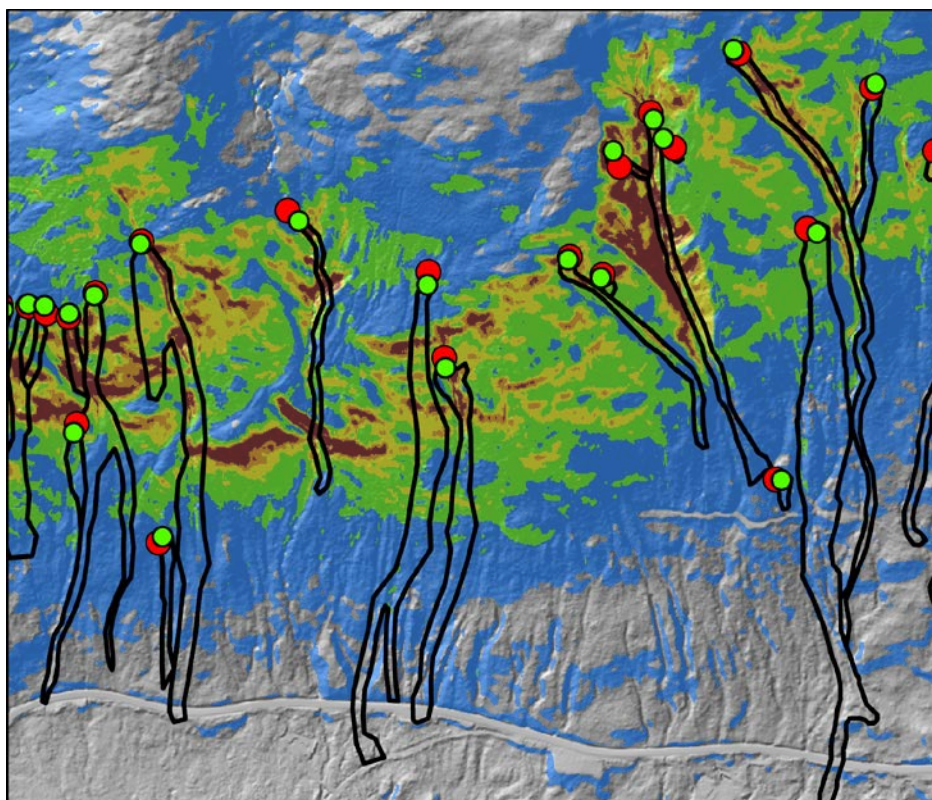
Figure 3. Landslide-initiation-point placement. Each landslide is associated with a single topographic index value at the inferred point of landslide initiation. The landslide inventory included both polygons and manually digitized initiation points, shown in green. Points automatically placed at the maximum index value found within the upper portion of each polygon are shown in red. The "upper" portion was defined as extending from the upper-most point downslope a distance equal to average polygon width through that portion.

Figure 4. Cumulative proportion of the analysis area (excluding areas with gradient less than 40%) and cumulative proportion of inventoried landslides versus topographic index. The analysis area has a greater abundance of lower index values than the landslide initiation points and the manually digitized points from the inventory have a greater abundance of lower index values than the points located by automated placement at the maximum index value within the upper portion of each landslide polygon.
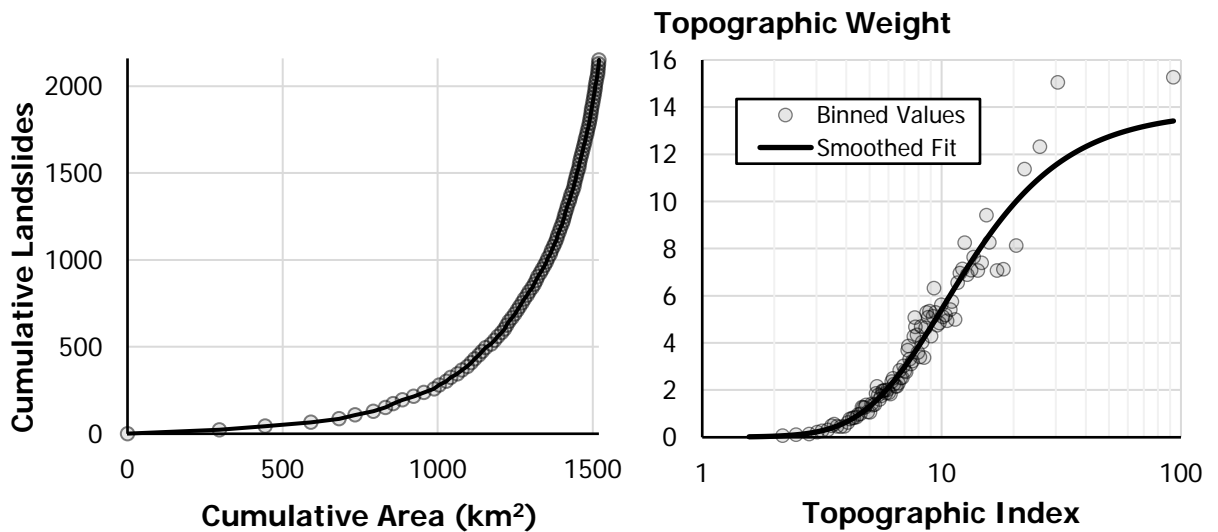
Figure 5. The left graph plots the cumulative area for each landslide, ranked by the topographic index for each landslide (shown as proportions in Figure 4). Each circle plotted along the curve corresponds to a single landslide and each landslide has an associated topographic index. The slope of this curve indicates landslide density (number of landslides found within a small increment of area) and location along the curve corresponds to topographic index.

Circles in the right graph show the slope calculated as one over the change in area for each landslide (dx/dy between each pair of circles in the left graph) divided by the mean landslide density over the analysis area to give topographic weight as defined in Equation (3). The solid line is a least-squares fit of a shifted logistic curve through those points. The smoothed curve provides topographic weighting as a function of the topographic index.

Topographic Weight
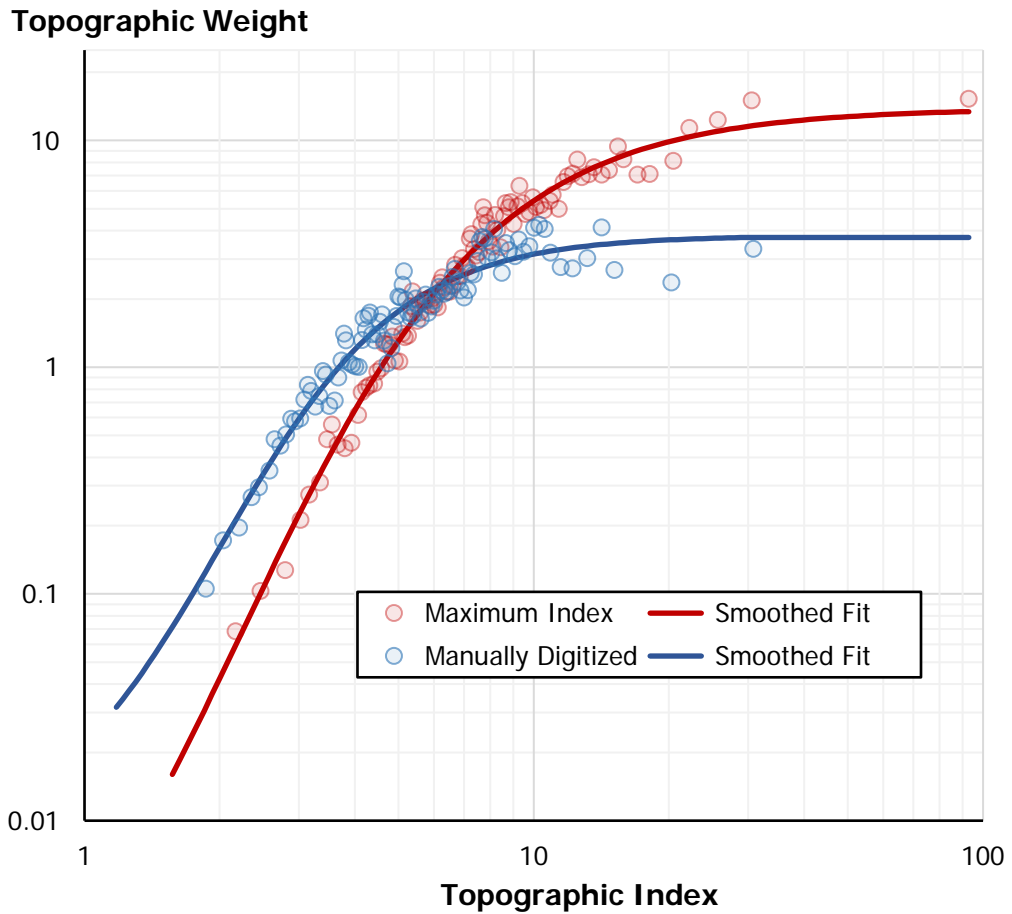
Figure 6. Topographic weighting curves obtained using the manually digitized landslide initiation points (blue) from the inventory and points automatically placed at the maximum topographic index value (red) within the upper portion of each landslide polygon. The average weight value over the analysis area is one in each case. Automated point placement results in lower weight values at small indices and higher weight values at larger indices than obtained with manually placed points. Manually placement is in reference to what is visible in aerial photos; automated placement is in reference to topography inferred from the Lidar DEM.
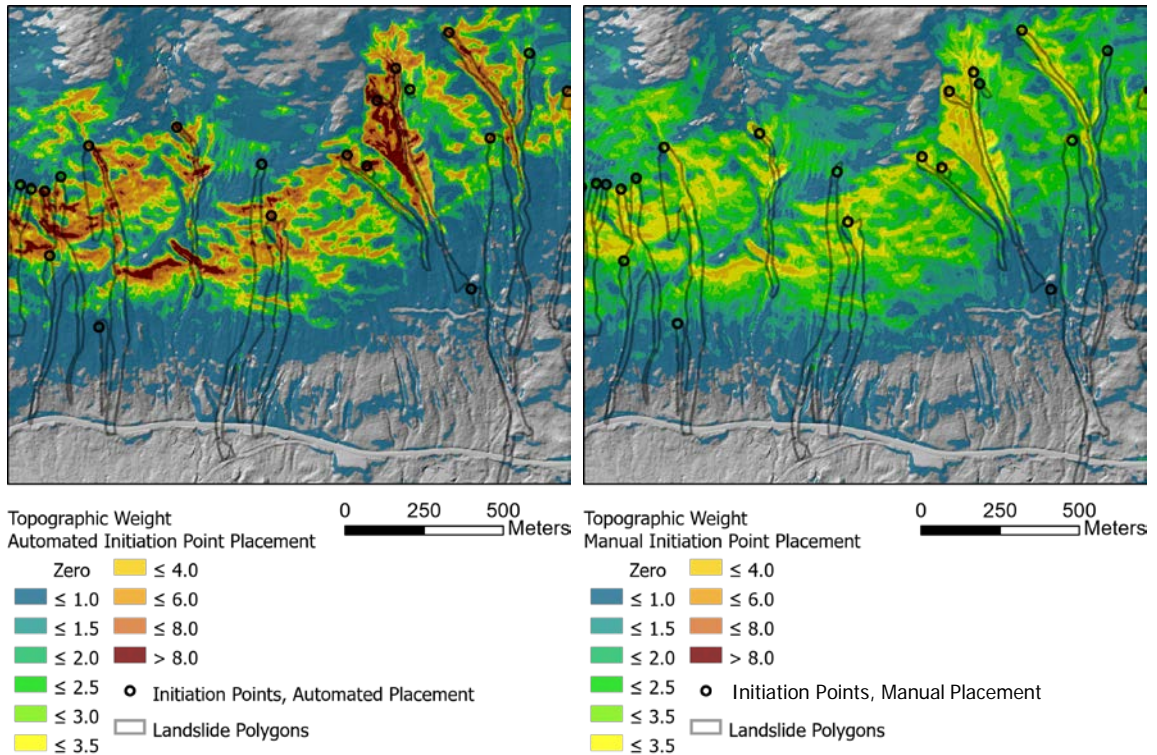
Figure 7. Spatial distribution of topographic weight values as obtained from both automated initiation point placement (left image) and manual placement (right). The distribution of high and low weight values are similar, but automated placement produces larger weighting in the high zones and lower weighting in the low zones than obtained with manual point placement. The contrast between high and low weight values is larger in the left image than in the right.

Harvest Year
▨	1962
▨	1963
▨	1969
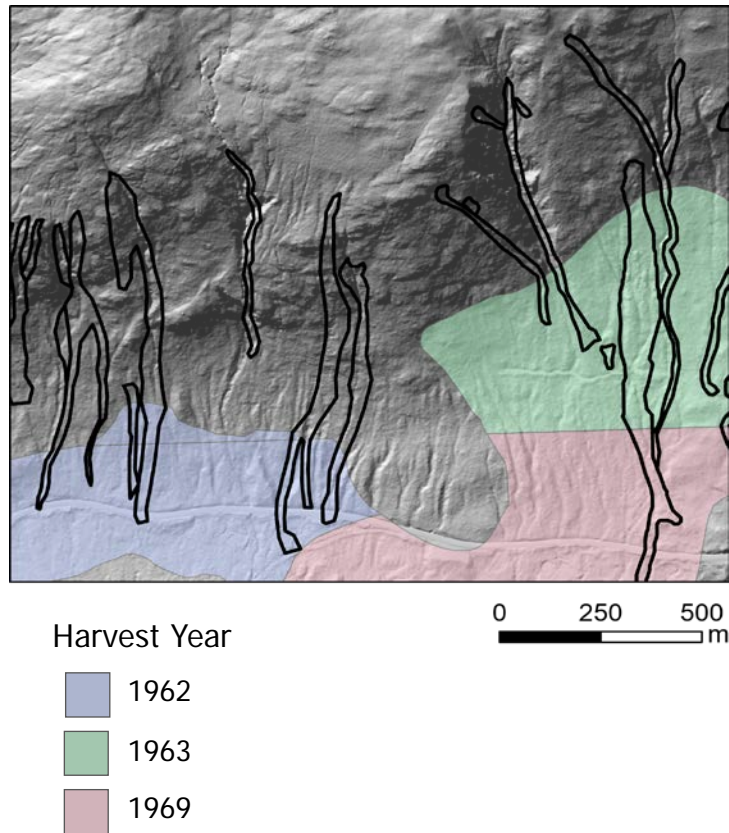
Figure 8. Harvest-unit polygons obtained from the
Tongass National Forest Management Activity database.
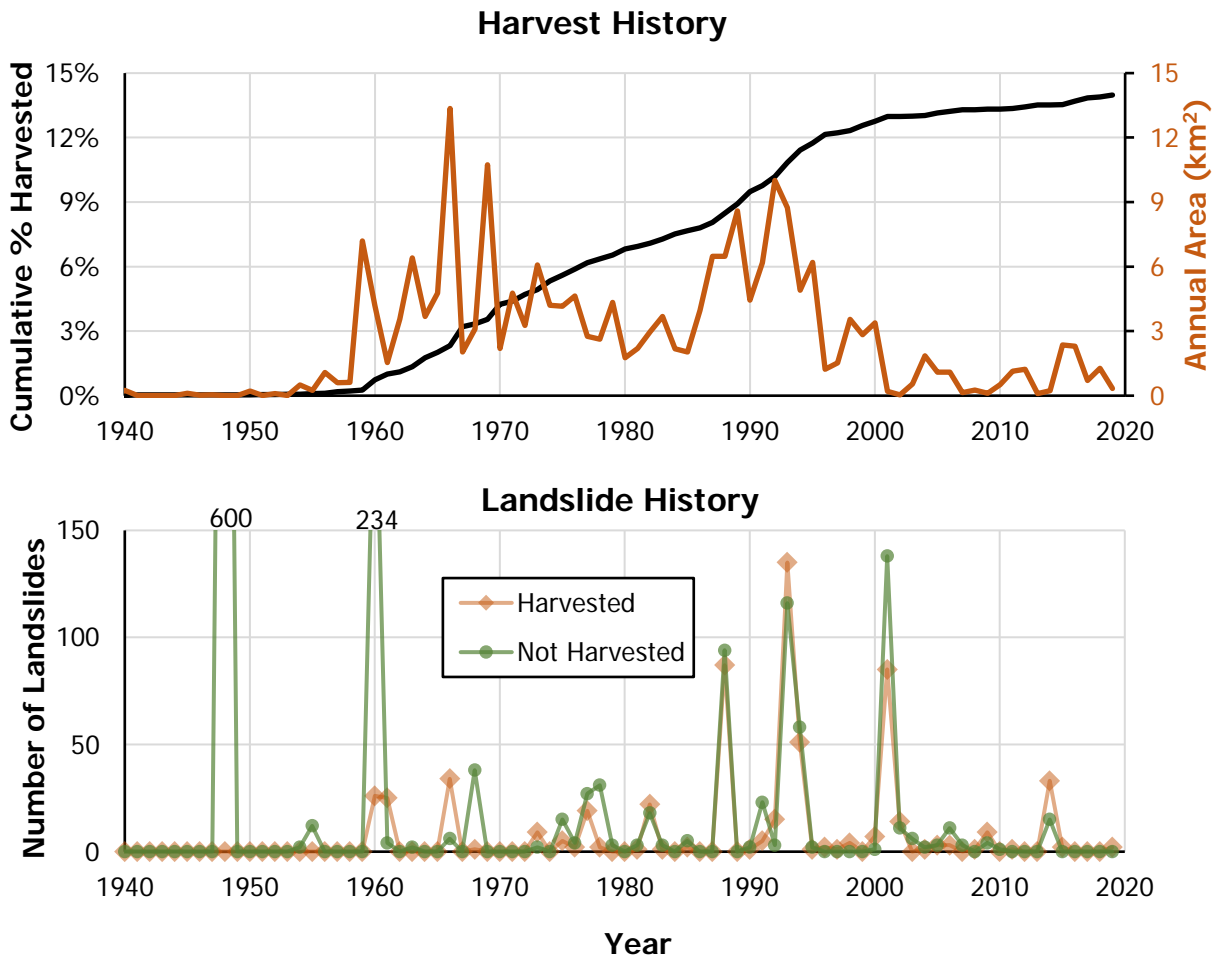
Figure 9. The upper graph shows the cumulative proportion of the analysis area harvested over time and the dark red line shows the area harvested each year. The lower graph shows the number of landslides recorded in the inventory over the analysis area each year, divided between those on previously harvested land and those on land not previously harvested. Substantial harvest started in 1959. Many landslide polygons were assigned dates of -1948 and -1960. Dates for these were uncertain and all these landslides were assumed to predate harvest at their locations.
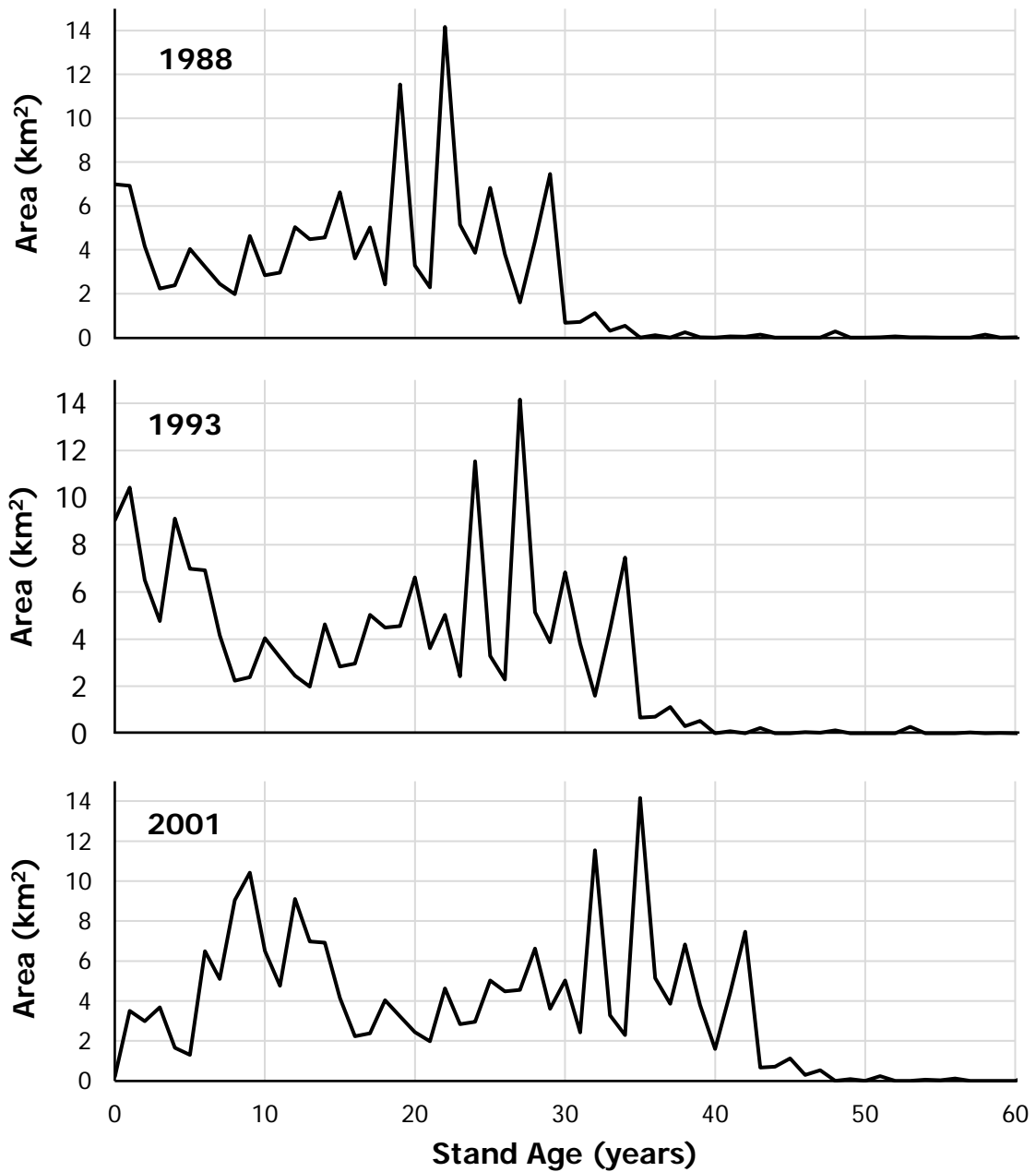
Figure 10. The area in stand ages up to 60 years in the three years with the largest number of landslides since 1960.
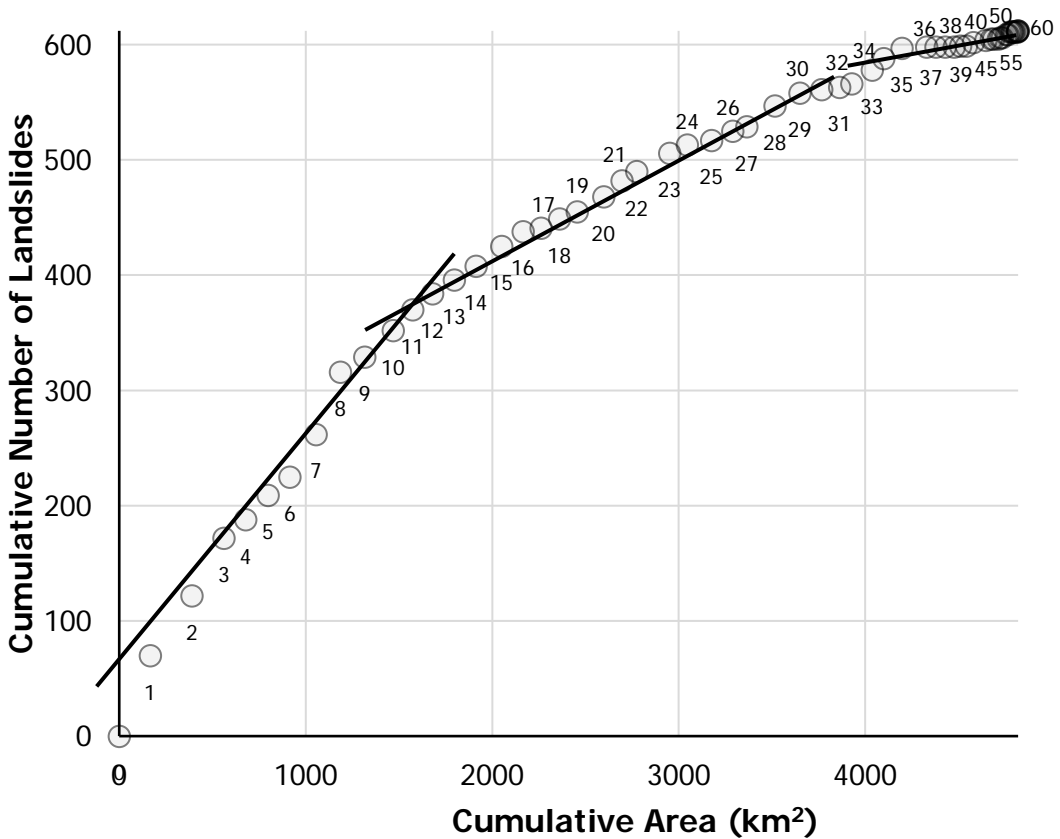
Figure 11. Cumulative area and cumulative landslides within harvested areas ranked by increasing stand age. The numbers by each circle indicate stand age. The slope of the curve defined by these points indicates landslide density; position along the curve indicates stand age. Together, these give landslide density for each stand age. The curve exhibits three zones of decreasing slope with increasing stand age: a steep portion extending from about zero to stand age 8-10 years, a less steep portion from about 10 to 30 years stand age, and a portion with small slope extending to older stand ages.
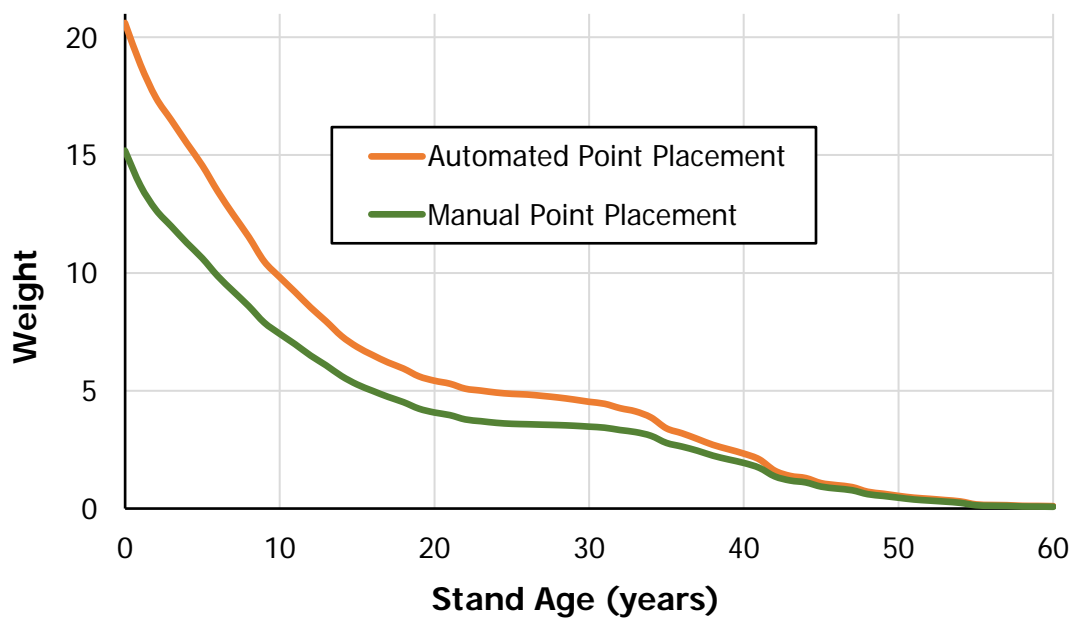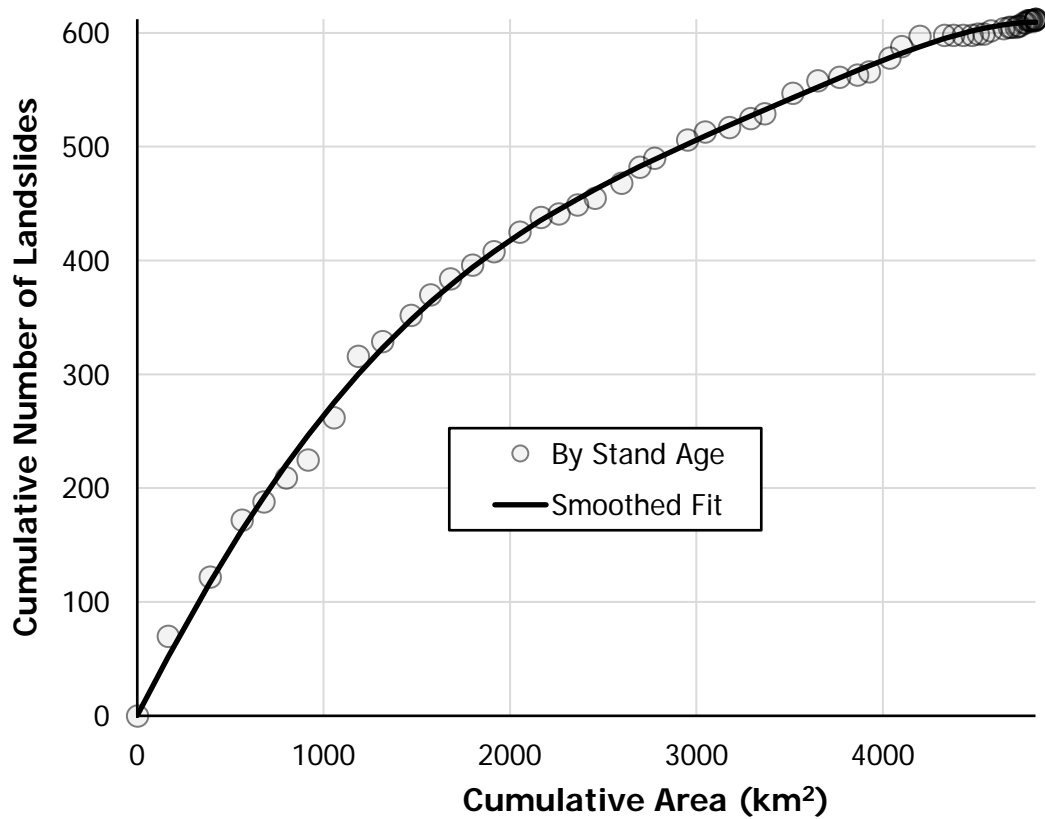
Figure 12. The upper graph shows a smooth curve fit through the points of Figure 11; the lower graph shows the slope of this curve, divided by the mean landslide density over the area of analysis to give weight (w_{AGE}), for each stand age from zero to 60 years.
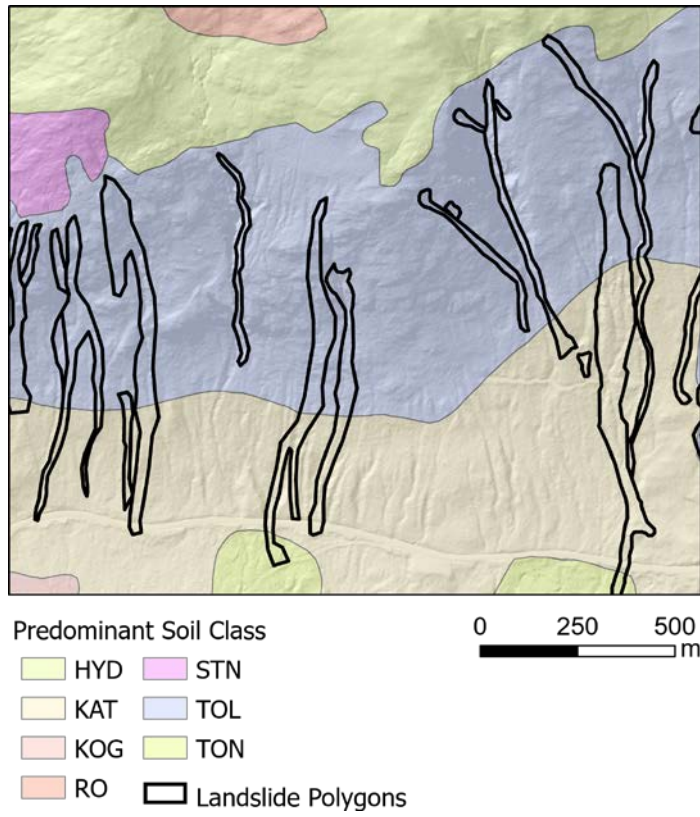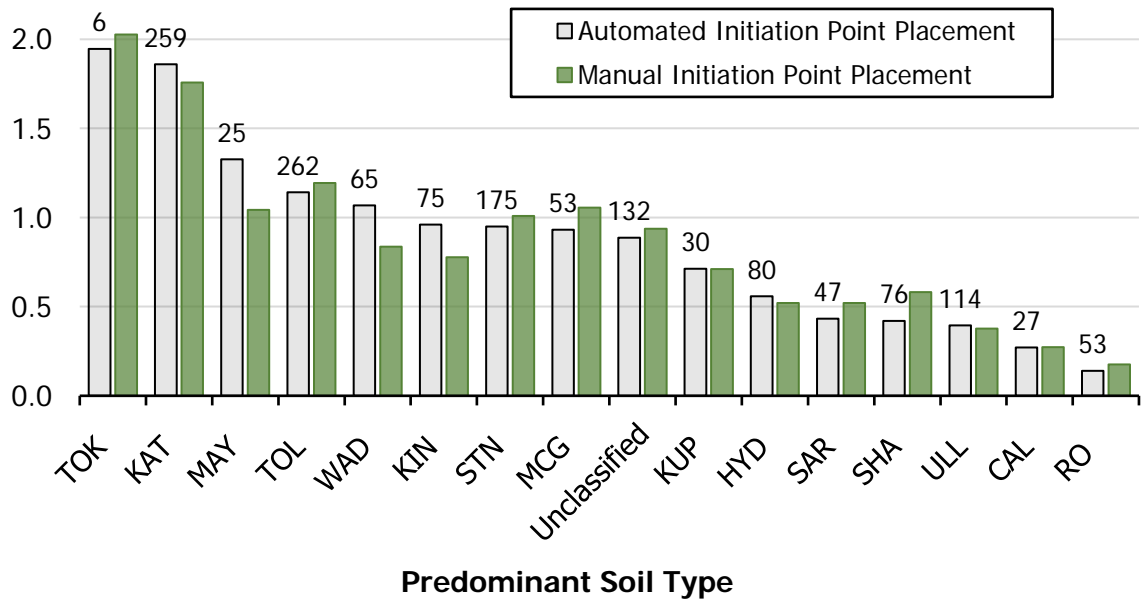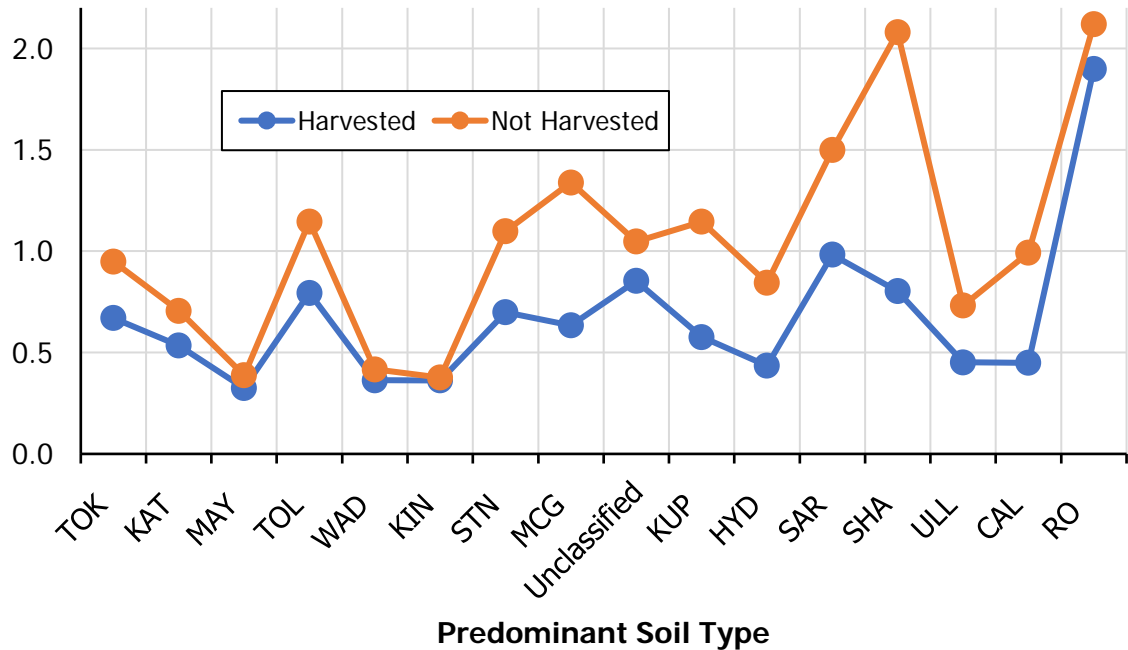
Figure 13. Soil-inventory polygons.

Area (km²)

Number of Landslides
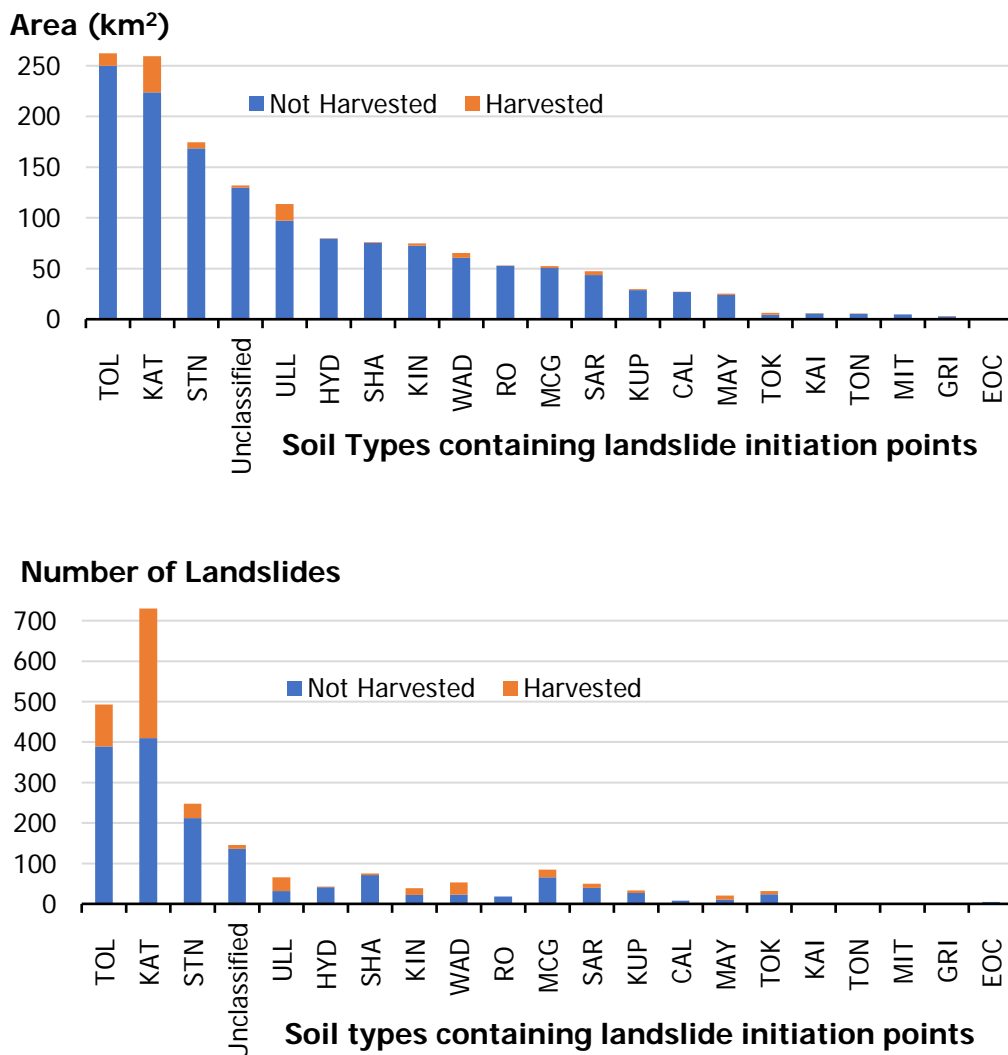
Figure 14. The area (upper graph) and number of landslide initiation points (lower graph) within each soil type, divided between areas harvested and not harvested.
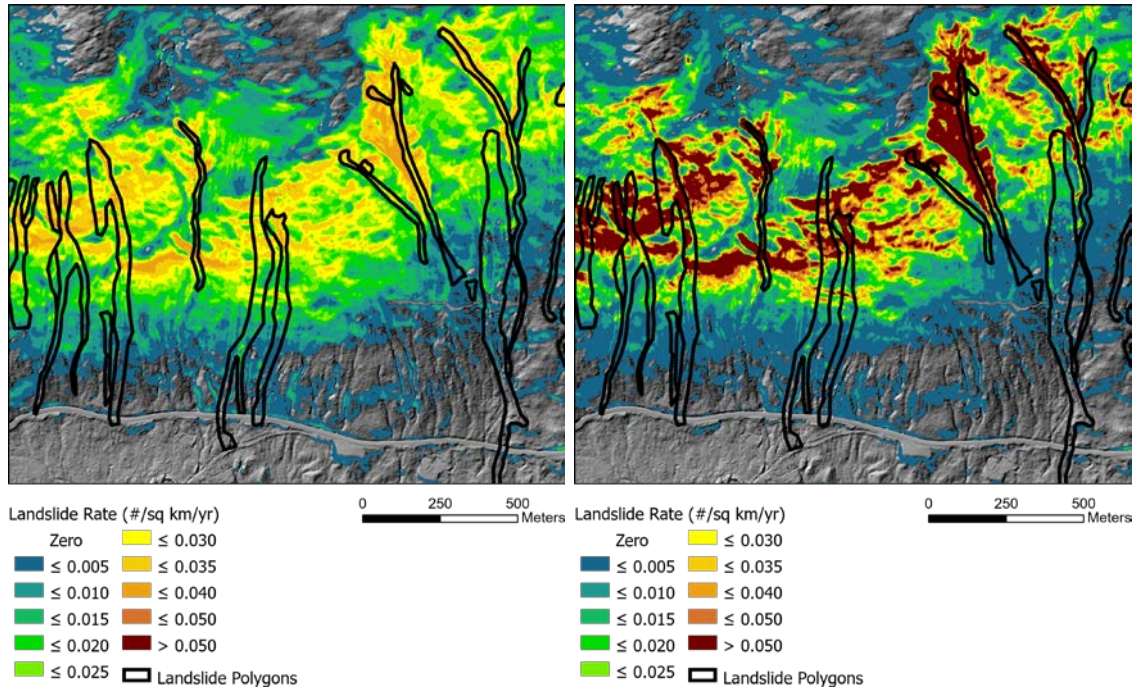
Figure 15. The upper bar graph shows weighting (w_S) inferred for each soil type with cumulative area greater than 6 km² that contain landslides. The lower graph shows the average topographic weighting for each soil type, divided between areas harvested and those not harvested.

Manual point placement   Automated point placement

Landslide Rate (#/sq km/yr)

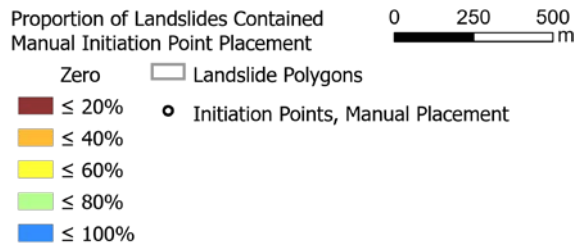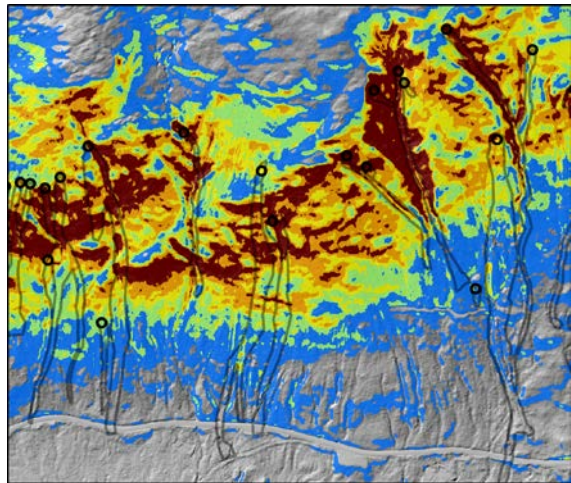|	Zero		≤ 0.030
	≤ 0.005		≤ 0.035
	≤ 0.010		≤ 0.040
	≤ 0.015		≤ 0.050
	≤ 0.020		> 0.050
	≤ 0.025		Landslide Polygons

Figure 16. Landslide rate in #/km^2/yr based on the abundance of landslide initiation points distributed over topographic attributes (partial contributing area times gradient) and soil types observed over a 91-year period. The left image shows results derived from manually digitized initiation points based on aerial photo interpretation. The right image shows results derived from automated initiation-point placement at the DEM cell with highest topographic index value within the upper portion of each landslide polygon. The spatial pattern of modeled high to low rate is the same in each image, but automated point placement produces greater contrast in the high-to-low-rate values.
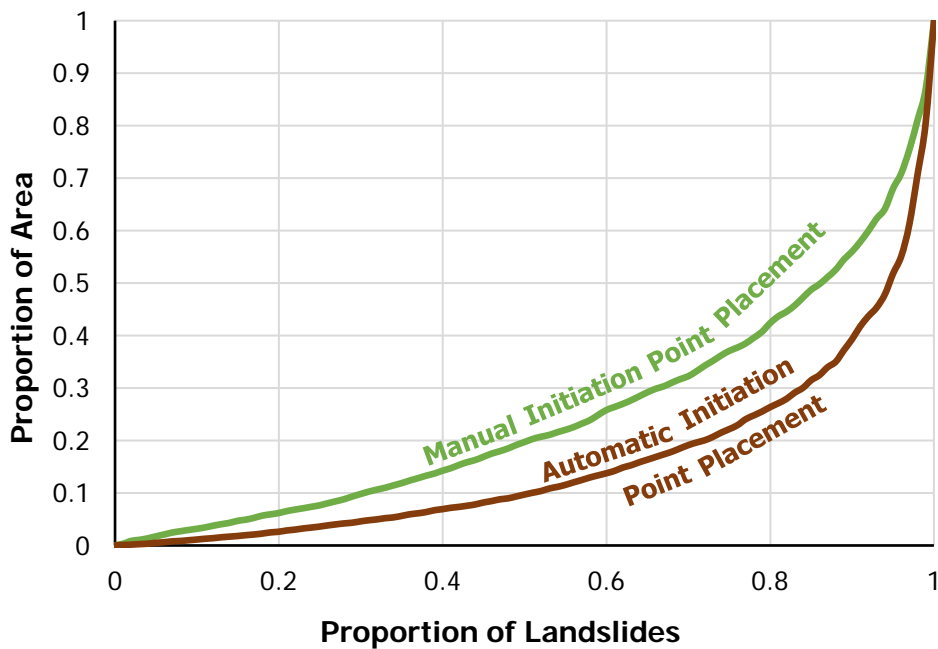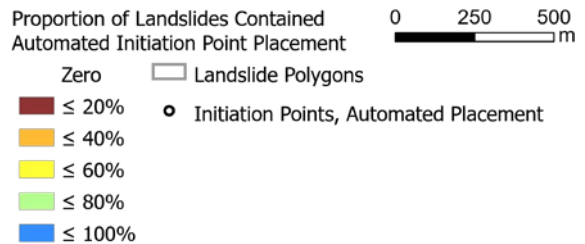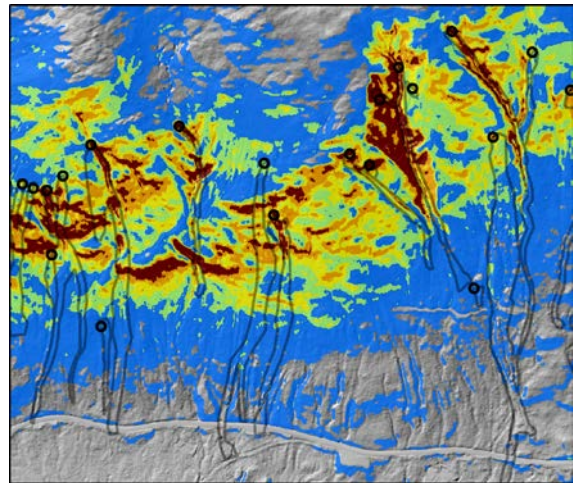
Figure 17. Proportion of landslides versus proportion of analysis area. This graph is similar to the left graph of Figure 5 except that the values have been normalized to show proportion of the total and the axes switched. A method that encompasses a greater proportion of landslides within a smaller area appears to better resolve landslide locations. If resolution is a criterion for choosing one model over another, automated point placement would appear to be the winning choice. But this difference in resolution is a consequence of how the initiation points were placed, so choice of the appropriate method should depend on which method of placement better represents actual landslide initiation zones.

Manual point placement

Automated point placement

Proportion of Landslides Contained
Manual Initiation Point Placement

0   250   500
m

Zero   ☐ Landslide Polygons
◼ ≤ 20%   ○ Initiation Points, Manual Placement
◼ ≤ 40%
◼ ≤ 60%
◼ ≤ 80%
◼ ≤ 100%

Proportion of Landslides Contained
Automated Initiation Point Placement

0   250   500
m

Zero   ☐ Landslide Polygons
◼ ≤ 20%   ○ Initiation Points, Automated Placement
◼ ≤ 40%
◼ ≤ 60%
◼ ≤ 80%
◼ ≤ 100%

Figure 18. Susceptibility in terms of the proportion of observed landslides. Position along the curves in Figure 17 corresponds to a particular landslide-rate value, so we can translate calculated rate to proportion of observed landslides. Each DEM cell has a calculated rate, so we can create a map delineating zones within increments of rate that contain a specified proportion of observed landslides. Here I've delineated zones within increments of landslide rate that each contain 20% of the observed landslide initiation points. Dark red delineates the highest-rate zone, blue delineates the lowest-rate zone. With automated point placement, the high-rate zones are smaller than those obtained with manual point placement. Likewise, with automated placement, the low-rate zones are larger.
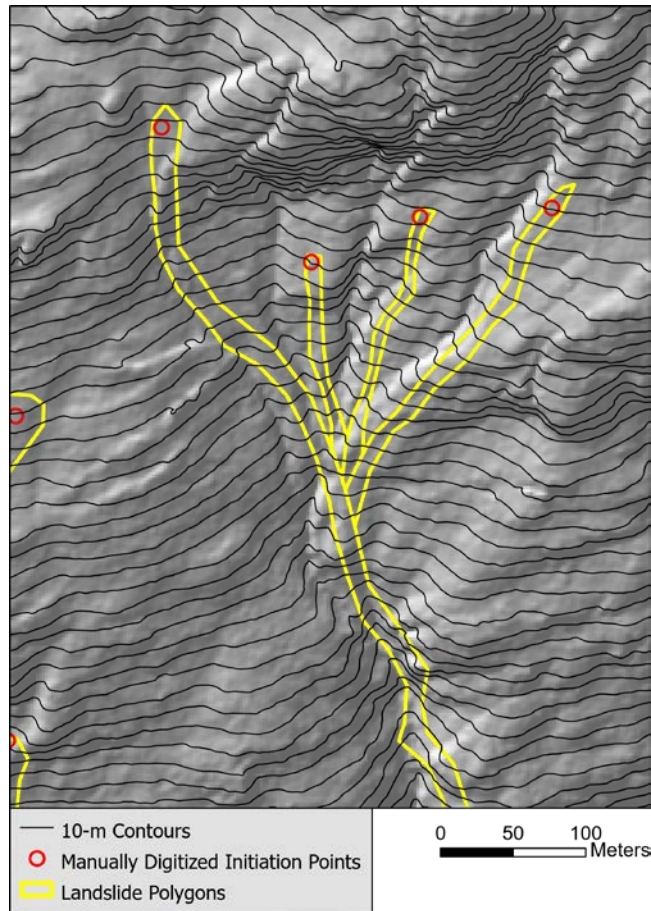
Figure 19. Discrepancies between the Lidar DEM and digitized landslide locations. The swales visible in the shaded relief image and contour lines are the most likely locations for landslide initiation and runout. The digitized landslide polygons and initiation points are in many places offset from these swales. Topographic attributes derived from the DEM and subsequently assigned to these landslides may not accurately represent the topography where the landslides occurred.

~90% Confidence Interval for background density of 1.0/km²
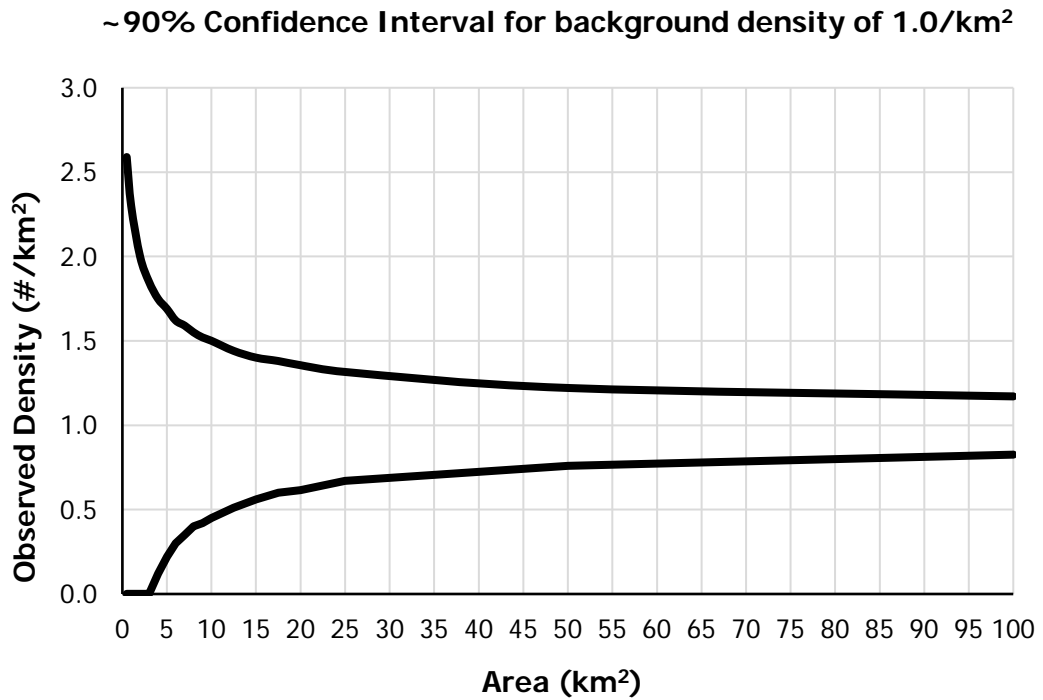
Figure 20. 90% confidence intervals estimated for observed landslide density as a function of area examined for a background landslide density of 1 per km2. If the area examined is small, there is little confidence that the observed value is an accurate estimate of the value that would be found if measured over a larger area.

Landslide Runout
Addendum to Landslide initiation susceptibility, Prince of Wales Island
Dan Miller, TerrainWorks
February 5, 2021

This addendum describes a simple method for estimating the potential that stream channels will be impacted by deposition of debris from upslope landslides. Two primary factors are used to assess this potential: 1) susceptibility to landslide initiation integrated over potential upslope landslide source areas, and 2) the distance of the source areas to a channel. The first factor was addressed in the body of the report. Here I examine runout lengths.

Potential runout length is characterized using the cumulative distribution of runout lengths measured from the set of polygons for debris-avalanche, debris-flow, and debris-torrent type landslides included in the Tongass National Forest landslide inventory for Prince of Wales Island. This characterization is applied to estimate probability of runout from every potential landslide initiation site delineated in the first part of this analysis to every point along the DEM-traced downslope flow path. The probability of landslide delivery is estimated for fish-bearing channels delineated here as all channels with no downslope gradient exceeding 8%.

Introduction
The cumulative distribution of horizontal runout length for all non-road-related debris-flow, debris-avalanche, and debris-torrent type landslide polygons is shown in Figure 21. This distribution is well fit by an exponential distribution and slightly better fit by a Weibull distribution. The exponential and Weibull distributions are used in survival analysis (e.g., Kleinbaum and Klein, 2012) to describe the expected time for some event to occur. If the rate of occurrence is constant, that is, if the probability of occurrence within any interval of time is the same no matter how much time has passed, then the observed distribution of wait times is described by an exponential distribution. The Weibull distribution describes the observed distribution if the rate of occurrence increases or decreases with time. Landslide runout length can be thought of in survival-analysis terms, with distance substituted for time Miller and Burnett (2008). If the probability that a landslide will stop over any increment of runout length is constant along a potential runout path, the observed distribution of runout lengths follows an exponential distribution. If the probability of stopping is proportional to the distance traveled, the observed runout lengths will follow a Weibull distribution. For landslides included in the Prince of Wales inventory, runout lengths are well described by an exponential distribution and by a Weibull distribution with a shape parameter of 1.05, suggesting that the probability of stopping within any increment of travel length is, on average, constant (0.0045/m) or nearly constant, increasing very slightly with distance traveled.

This observation seems somewhat surprising. One might expect that the downslope extent of debris flow or landslide runout will depend on many factors: the volume of debris (Griswold and Iverson, 2008), the surface gradient and the degree of topographic confinement (Fannin and Rollerson, 1993), the number and size of trees encountered and the resulting amount of large wood in the debris (Booth et al., 2020). These factors may all influence the probability of stopping, yet the results shown in Figure 21 suggest that the *aggregate* behavior of landslides on Prince of Wales Island is well described with a

constant, or nearly constant, stopping rate. I use that result here to provide a first-cut estimate of runout potential. After examining these results, I will discuss analyses that we might try to better account for site-specific attributes.

Methods

Using the initiation susceptibility analysis described in the main body of the report, each DEM cell is assigned a landslide density. Density times area gives number of landslides, or for a DEM cell, the probability P_I that the cell contains a mapped initiation point:

$$P_I = \rho a$$

where P_I is the initiation probability for a DEM cell, ρ is the landslide density calculated for the cell, and a is cell area. The DEM-derived topography defines a probable flow path downslope from each potential initiation point. The probability P_R that a landslide or debris flow initiated reaches any point along that flow path starts at one at the initiation point and decreases with distance at a rate defined by the Weibull distribution fit shown in Figure 21:

$$P_R = e^{(\lambda(L-L_0))^\alpha}$$

Here L is horizontal runout length, L_0 is the length of the shortest landslide polygon in the inventory (P_R is one for $L \le L_0$), λ indicates the probability that runout ceases along any increment of travel, and α determines how much that probability changes with runout length. The probability that a DEM cell along that runout path is within a mapped landslide polygon is estimated as the initiation probability times the runout probability: $P_I P_R$. If a stream channel of interest is encountered along the runout path, the value of $P_I P_R$ at that point indicates the probability that a landslide initiated at the upslope DEM cell ran out to that channel. That probability value is then assigned to the upslope initiating DEM cell. This procedure is repeated for every upslope DEM cell to build a raster showing the modeled probability for a landslide initiated at each cell to travel to a channel of interest, such as a fish-bearing stream. The landslide density raster computed using the methods previously described can then be multiplied by this delivery-probability raster to give a raster showing the modeled density of initiation points for landslides that can deliver material to the channels of interest.

To estimate probability that any point in the channel network is traversed by or receives a landslide or debris-flow deposit requires tracing every potential flow path from every potential initiation point and tracking the probability along that flow path. For any single initiation point, the probability is as described above: $P_I P_R$, from which the probability that a point along the potential flow path was not impacted by a debris flow is 1 - $P_I P_R$. At any point in the channel network, there may be many – hundreds, perhaps thousands – of potential initiation points, each of which could produce a landslide that reaches that point in the channel. The combined probability that none of those initiation points triggered a landslide that reached that channel is the product $\prod_{i=1}^{n}(1 - P_I P_R)_i$ where n is the total number of upslope initiation points. The probability that a debris flow did impact that point in the channel network is then

$$1 - \prod_{i=1}^{n}(1 - P_I P_R)_i \qquad\qquad (A1)$$

This value is calculated for every DEM cell.

Two observations can also be used to constrain total runout length. Landslide runout for a population of landslides can be characterized in terms of empirical mobility indices (Hungr et al., 2005). Most of these require estimates of the deposit volume, which is unknown for this analysis, but the "angle of reach", defined as the ratio of vertical relief H divided by the horizontal length L from the top of the failure zone to the distal end of the deposit provides an index based solely on topography. I use the minimum angle-of-reach value found for the landslide polygons in the inventory to constrain potential runout length: if the H/L value along any potential runout path becomes less than the observed minimum, probability of runout beyond that point is set to zero. Additionally, probability of runout is set to zero for runout lengths beyond the maximum found for the landslide polygons in the inventory.

These methods produce two rasters: probability of delivery to a channel of interest and density of initiation sites of landslides that could travel to a channel of interest. A raster showing the probability that a DEM cell is traversed by a debris flow initiated upslope that continued to a channel of interest can also be produced, but was not needed for this analysis. A vector file of the channel network giving the probability for debris-flow or landslide deposition in a channel, calculated with Equation (A1), is also produced.

Estimates of delivering landslide density and probability of in-channel deposition are, however, contingent on the number of landslides included in the inventory, which is contingent on the period of time spanned by landslide events in the inventory. To remove this dependence on the size of the inventory, susceptibility is measured in terms of the proportion of delivering landslide initiation sites and the proportion of impacted channel length.

For initiation sites, this proportion is calculated from the modeled landslide density. Density times area gives expected number of landslides. For some set of n DEM cells, summing the product of modeled density (ρ) for each cell and cell area (a) over all n cells gives the number of landslides (N_{LS}) expected within the area encompassed by those cells: $N_{LS} = \sum_{i=1}^{n} a\rho_i$. The proportion of mapped landslide initiation sites encompassed within areas of increasing modeled density is found by ranking cells by density and then summing values from low to high to give a cumulative distribution, which is then divided by the total sum:

$$P_j = \frac{\sum_{i=1}^{j} \rho_i}{\sum_{i=1}^{n} \rho_i} \qquad (A2)$$

P_j gives the proportion of landslide initiation sites encompassed within areas having modeled density less than or equal to ρ_j. The proportion P_D of initiation sites for landslides that can potentially deposit material in fish-bearing streams, for example, is then found as

$$P_{Dj} = \frac{\sum_{i=1}^{j} \rho_i P_{Ri}}{\sum_{i=1}^{n} \rho_i P_{Ri}} \qquad (A3)$$

where P_{Dj} is the proportion of delivering initiation sites encompassed within areas having modeled delivered density less than or equal to $\rho_j P_{Rj}$.

A similar procedure is used for stream channels. Just as a DEM discretizes the landscape into a grid of points, with each point having an associated area and set of attributes (e.g., elevation, gradient), the channel network is discretized into a set of points, with each point having an associated channel length

and set of attributes (e.g., channel gradient, contributing area). I refer to the channel points as nodes. The data structure used to represent a channel network is a set of linked nodes, so attributes for each node include the ID of adjacent up- and downstream nodes. The channel network is derived from flow paths traced on the DEM, so a channel node is defined for each DEM cell that meets the criteria of being a channel. The digital representation of a channel network is then at the same spatial resolution as the DEM from which it was derived. When a landslide flow path is traced downslope from a potential initiating site, once it intersects DEM cells classified as channels, the modeled runout probability is used with Equation ($A1$) to assign a probability of landslide deposition to that node.

Every channel node thus has an associated modeled probability of receiving material from an upslope landslide. When viewed over the channel network, this probability can be interpreted in terms of density: the length of channel receiving deposits per unit channel length. For a set of n channel nodes, the product of modeled landslide probability $P(LS)$ and channel length l associated with a node, summed over all nodes in the set, gives the expected length CL_{DEP} of channel with landslide deposits: $CL_{DEP} = \sum_{i=1}^{n} P(LS)_i l_i$, where $P(LS)_i$ and l_i are the modeled landslide probability and channel length associated with the ith node. Ranking nodes for the entire channel network by landslide probability and summing the product over all nodes, from low to high landslide probability, provides a cumulative distribution of expected deposit length. Dividing by the total sum gives the proportion P_{Dep} of deposit length as a function of modeled landslide probability:

$$P_{DEPj} = \frac{\sum_{i=1}^{j} P(LS)_i l_i}{\sum_{i=1}^{n} P(LS)_i l_i} \tag{A4}$$

P_{DEPj} gives the proportion of channel length with landslide deposits (length intercepting mapped landslide polygons) with modeled landslide probability less than or equal to $P(LS)_j$.

These proportions, P_D for delivering initiation sites and P_{DEP} for in-channel landslide deposits, provide quantitative and testable measures of susceptibility. These measures can also be used in cost-benefit types of analyses, showing the proportion of initiation sites or the proportion of affected channel length encompassed under different upslope and riparian management scenarios.

Results

Figure 21A shows the cumulative distribution of runout lengths measured from the landslide polygons in the Tongas National Forest inventory. The maximum-likelihood (least squares) fit to a Weibull distribution is included in the figure. Figure 21B shows the cumulative distribution of angle-of-reach (H/L) values measured for these polygons. The minimum H/L value observed is 0.11. The largest runout length was 2152 meters.

To illustrate use of these methods, I estimated the upstream extent of the fish-bearing channel network as extending to channels with no downstream gradient exceeding 8%. Channel gradient was estimated at each channel node by fitting a straight line through a channel profile centered at each node and extending a total length of 20 channel widths. Channel width was estimated using regional regressions to contributing area and mean annual precipitation. Delivery probability to the delineated channels was calculated for every DEM cell having a modeled landslide density greater than zero. The modeled pattern of delivery probability is shown for a small portion of the study area in Figure 22A. Initiation sites close to channels have high delivery probability; sites far from channels have low delivery

probability. Figure 22B shows susceptibility to landslide initiation in terms of proportion of initiation sites for all landslides, including those that may not deliver material to those delineated fish-bearing streams. Figure 22C shows susceptibility to landslides that may deliver material in terms of the proportion of potentially delivering sites. Comparing Figures 22B and 22C it is apparent that modeling suggests a large proportion of potential initiation sites are too far from fish-bearing channels to act as source areas for landslides to these channels.

Figure 22C shows channels color coded in 20% increments of P_{DEP} from Equation (A4). Black-colored channels have zero modeled probability. Each color encompasses channels that contain 20% of the total in-channel deposit length (over the entire study area) and colors indicate ranking from high landslide probability (yellow) to low (purple). The channel ranking is determined by the number and ranking of upslope delivering landslide initiation sites and the distance of these sites from the channel. Figure 23 shows the channel rankings for fish-bearing streams (gradient <8%) for the entire study area.

Discussion

The modeled results depend explicitly on the portion of the channel network delineated. A similar exercise could be done to look at delivery to and depositional probability to all channels, or just to channels with particular habitat attributes, or to a water-supply reservoir, for example. An analysis can be tailored to the questions at hand.

This analysis has treated all potential runout paths the same, but other studies indicate that runout length may depend on a variety of potentially measurable attributes. Deposit volume is a primary determinant of runout length; most empirical methods for estimating runout use estimates of volume. For example, Iverson et al. (1998) show that the area of inundation for volcanic lahars is proportional to the deposit volume taken to the 2/3 power. This relationship was used to develop the Laharz algorithm for GIS-based mapping of susceptibility to inundation by volcanic lahars (Schilling, 1998). Griswold and Iverson (2008) extended the empirical analysis to include debris flows and rock avalanches. The Laharz algorithm thus provides a means of estimating runout extent for specific initiation sites if the deposit volume can be estimated. Hofmeister and Miller (2003) coupled Laharz with volume estimates based on integrated scour length of modeled debris-flow tracks to generate debris-flow-hazard maps for Western Oregon (Hofmeister et al., 2002). Reid et al. (2016) used a similar approach, but with much more detailed topographic control on scoured volume to calibrate a debris-growth function for debris flows in the Oregon Coast Range.

If topographic constraints on where landslides tend to scour material and thus grow in size can be defined for southeast Alaska, perhaps a similar approach could be developed here. Johnson et al. (2000), for example, report on rates of scour (volume/area) field-measured as functions of slope gradient and forest cover for landslides on Prince of Wales Island. This type of data could potentially be used to develop debris-growth functions here. A large storm last October triggered many landslides on the island. We have high-resolution Lidar-based topography pre-storm; collection of post-storm Lidar could be used for DEM differencing to estimate volume and build debris-growth rate functions following the example of Reid et al., (2016).

Booth et al. (2020) present observations suggesting that runout length for landslides in southeast Alaska is inhibited by the presence of large wood in the deposits. This suggests that runout length may be associated in some way with characteristics of the forest stand crossed by a landslide (see also Johnson

et al., 2000). For landslides that traversed areas with timber harvest, an analysis using the Tongass National Forest Activity database may be used to look for associations between runout length and stand age similar to what was done in the main report to look for associations with landslide initiation-site density.

Citations

Booth, A. M., Sifford, C., Vascik, B., Siebert, C., and Buma, B., 2020, Large wood inhibits debris flow runout in forested southeast Alaska: Earth Surface Processes and Landforms.

Fannin, R. J., and Rollerson, T. P., 1993, Debris flows: some physical characteristics and behavior: Canadian Geotechnical Journal, v. 30, no. 1, p. 71-81.

Griswold, J. P., and Iverson, R. M., 2008, Mobility statistics and automated hazard mapping for debris flows and rock avalanches: U.S. Geological Survey.

Hofmeister, R. J., and Miller, D. J., 2003, GIS-based modeling of debris-flow initiation, transport and deposition zones for regional hazard assessments in western, Oregon, USA, *in* Reickenmann, and Chen, eds., Debris-Flow Hazards Mitigation: Mechanics, Prediction, and Assessment: Rotterdam, Millpress, p. 1141-1149.

Hofmeister, R. J., Miller, D. J., Mills, K. A., Hinkle, J. C., and Beier, A. E., 2002, Hazard map of potential rapidly moving landslides in western Oregon, Interpretive Map Series - 22: Oregon Department of Geology and Mineral Industries.

Hungr, O., Corominas, J., and Eherhardt, E., 2005, Estimating landslide motion mechanism, travel distance and velocity, *in* Hungr, O., Fell, R., Couture, R., and Eberhardt, E., eds., Landslide Risk Management: London, Taylor & Francis Group.

Iverson, R. M., Schilling, S. P., and Vallance, J. W., 1998, Objective delineation of lahar-inundation hazard zones: Geological Society of America Bulletin, v. 110, p. 972-984.

Johnson, A. C., Swanston, D. N., and McGee, K. E., 2000, Landslide initiation, runout, and deposition within clearcuts and old-growth forests of Alaska: Journal of the American Water Resources Association, v. 36, no. 1, p. 17-30.

Kleinbaum, D. G., and Klein, M., 2012, Survival Analysis. A Self-Learning Text, Springer.

Miller, D. J., and Burnett, K. M., 2008, A probabilistic model of debris-flow delivery to stream channels, demonstrated for the Coast Range of Oregon, USA: Geomorphology, v. 94, p. 184-205.

Reid, M. E., Coe, J. A., and Brien, D. L., 2016, Forecasting inundation from debris flows that grow volumetrically during travel, with application to the Oregon Coast Range, USA: Geomorphology, v. 273, p. 396-411.

Schilling, S. P., 1998, LAHARZ: GIS programs for automated mapping of lahar-inundation hazard zones: U.S. Geological Survey, Open-File Report 98-638.
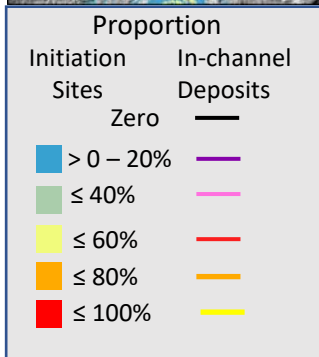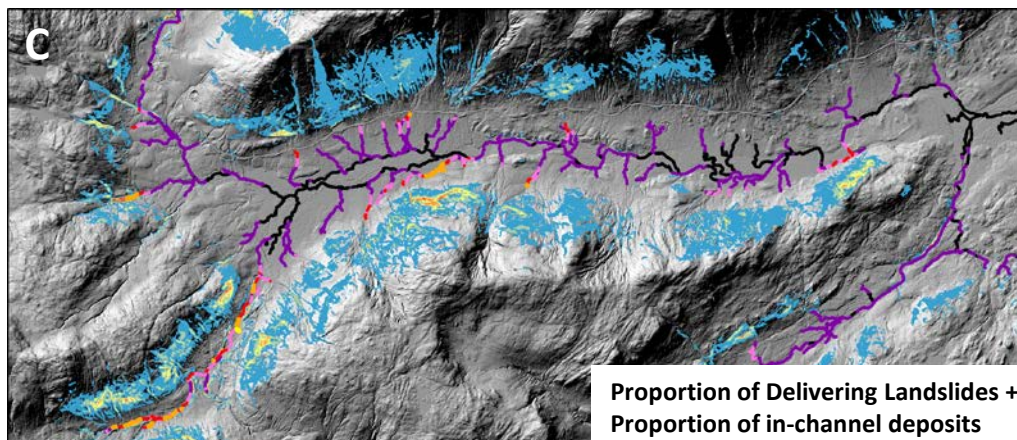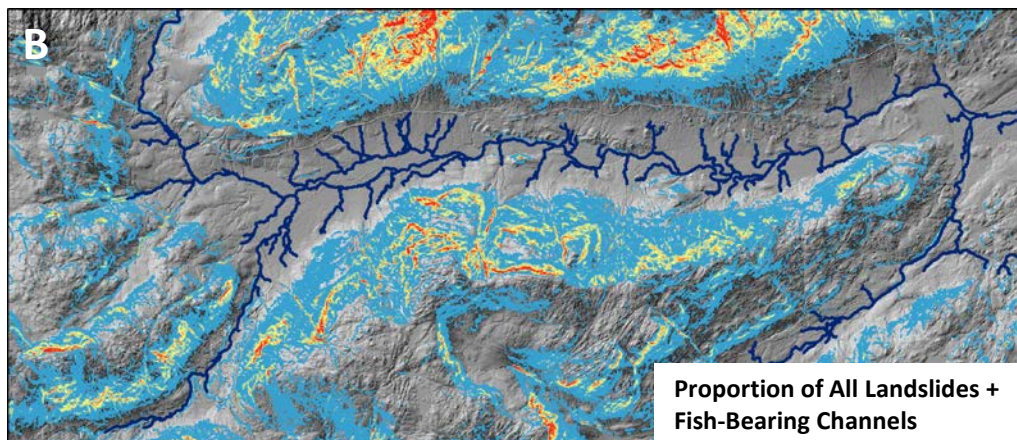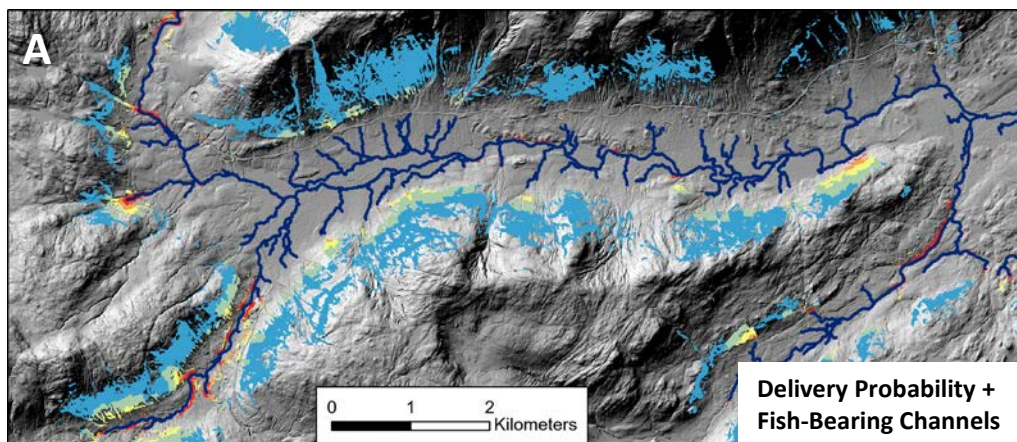
A. Distribution of Horizontal Runout Lengths

$$y = 1 - e^{(\lambda(L-L_0))^\alpha}$$
$\lambda = 0.00453$
$L_0 = 16.0$
$\alpha = 1.047$
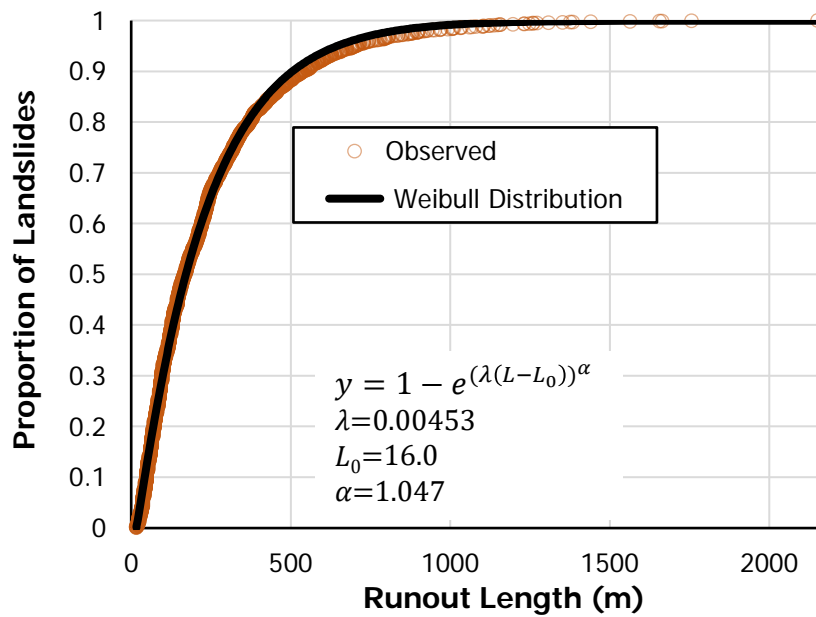
B. Distribution of angle-of-reach
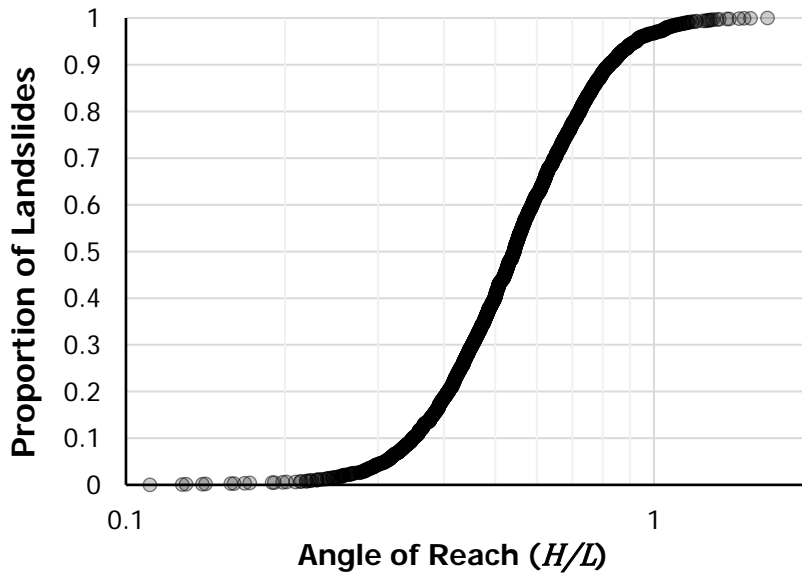
Figure 21. Runout statistics for landslide polygons.

A Delivery Probability +
Fish-Bearing Channels

B Proportion of All Landslides +
Fish-Bearing Channels

C Proportion of Delivering Landslides +
Proportion of in-channel deposits

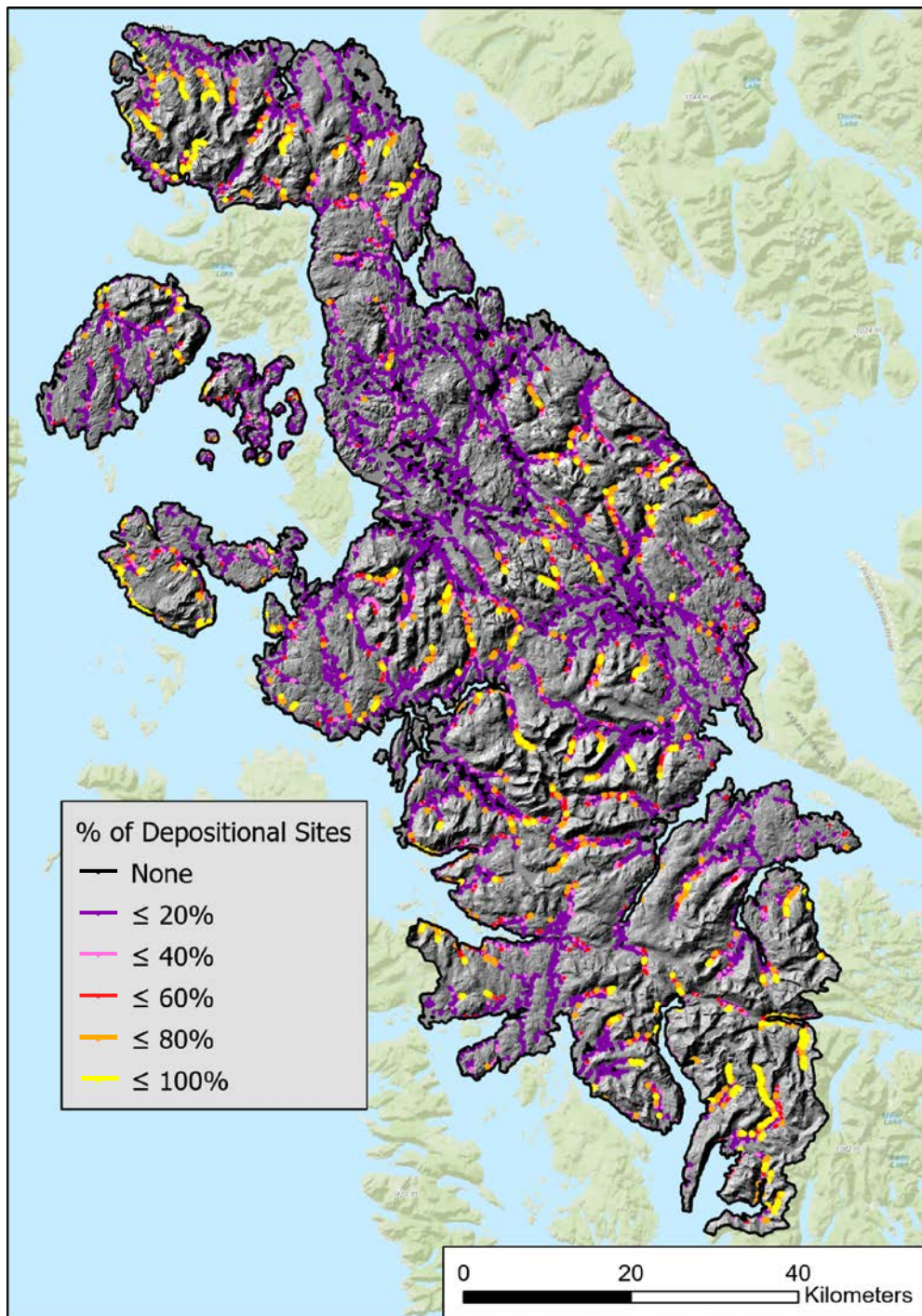| Proportion	
Initiation Sites	In-channel Deposits
Zero	—
> 0 – 20%	—
≤ 40%	—
≤ 60%	—
≤ 80%	—
≤ 100%	—

Figure 22A. Probability of delivery to a fish-bearing channel for every potential initiation point. Zero probability is uncolored; fish-bearing channels shown by dark-blue lines, estimated as all channels with no downslope gradient exceeding 8%.
B. Zones delineating terrain by proportion of all landslide initiation sites.
C. Zones delineating terrain by proportion of delivering landslide initiation sites. Channels color-coded by proportion of all in-channel landslide deposits.

Figure 23. Channel classified in terms of the cumulative proportion of in-channel landslide deposits.